FACULTY OF SCIENCE – CHARLES UNIVERSITY PRAGUE

IVAN ŘEHOŘ

TITANIUM DIOXIDE – PHOSPHONATE ASSEMBLIES AS MEDICAL NANOPROBES

PHD. THESIS

Prague 2011

Author declares that he did not use this work or its substantial part to acquire any academic title.

I. – Introduction 4
I.1 – Medical Imaging 4
I.2 – Nanoscale Medical Probes 7
I.3 – Adsorption of Phosphonic Acid Derivatives onto Oxidic Surfaces, Namely TiO_2 9
I.4 – Photocatalytic Properties of TiO_2 11
II. – Aim of the Work 12
II.1 – Step one: Proof of the Principle 12
II.2 – Step two: Mastering of Adsorption Process and Colloidal Stability 13
II.3 – Step three: Preparation of Biologically Applicable Multimodal Probe 13
II.4 – Step four: Exploitation of TiO_2 Photoactivity for Cancer Therapy 14
III. – Discussion of the Results 15
III.1 – Step One: Proof of the Principle 15
III.1.1 – Ligand DOTAPP Synthesis and Properties of its Ln(III) Complexes 16
III.1.1 – Adsorption of GdDOTAPP onto TiO_2 Surface 17
III.2 – Step two – Mastering the Colloidal and Adsorption Chemistry 18
III.2.1 – Adsorption Capacity 20
III.2.2 – Phosphonate/Bisphosphonate Co-adsorption 22
III.2.3 – Desorption Experiments 23
III.3 – Step 3: Bioapplicable Multimodal Nanoprobe 26
III.3.1 – Preparation and Properties of MRI and OI functionality 27
III.3.2 – Preparation and Properties of Nanoprobe TiO_2@RhdGd 28
III.3.3 – Labeling of Stem Cells 30
III.3.4 – Labeling of HeLa Cells 31
III.3.5 – Homing of TiO_2@RhdGd Labeled Leukocytes in-vivo 33
III.3.6 – Labeling of Pancreatic Islets 34
III.4 – Step four: Photocatalytic activity of TiO_2@RhdGd 37
IV. – Conclusion 39
V. – Experimental Details 41
V.1 – Preparation of Ligand DOTAPP its Ln(III) Complexes and TiO_2@GdDOTAPP (reaction scheme on page 15) 41
V.2 – Adsorption Study Experiments 43
V.3 – Preparation of TiO_2@RhdGd 43

I. – Introduction

Rapid development in medicine gave rise to wide scale of so called "medical agents", advanced chemicals, which are designed for various tasks in patient's body. We meet these agents in crucial areas of modern medicine and research, being used in therapy *e.g.* in drug delivery and drug release systems as well as in diagnosis. Special agents are used for recognition of pathologies or detection of specific processes. These agents are usually designed so that their presence (or activity) can be detected with particular medical imaging method.

I.1 – Medical Imaging

Diagnostic imaging methods are able to noninvasively display inside of patients body and are powerful tool in hands of contemporary medicine. The methods in scope of this text are Computed Tomography (CT), Magnetic Resonance Imaging (MRI), Positron Emission Tomography (PET), Single Photon Emission Tomography (SPECT) and Optical Imaging (OI). All these methods are based on detection of electromagnetic radiation, each at particular wavelengths – x-ray in CT γ-rays in PET and SPECT, visible light and near IR in OI and radiofrequency waves in MRI. The signal is acquired with spatial resolution and final image is created as signal intensity in particular space element. Medical agents, which are used in imaging, are called contrast agents (CA). Some of imaging methods, namely MRI and CT can be used even in absence of contrast agent, in the others, presence of CA is necessary. The molecule of the contrast agent contains specific group (radioisotope for SPECT and PET or paramagnetic ion/particle for MRI), which can be detected in corresponding imaging method. When contrast agent is administered, the intensity of the signal obtained by scanner is proportional to local CA concentration. Therefore it is necessary to achieve specific CA distribution among particular types of tissues for their visualization.

Radiomethods (PET, SPECT, CT) are based on spatially resolved radiation detection. The radiation source is external in the case of CT and angle dependency of intensity of x-ray passing through the patient's body is transferred to 3D image. Contrast agents, composed from atoms with large intersection (iodine based CAs, barium sulfate) are often used, but not necessary. CT is the most widely spread method from all discussed in this section. Although the spatial resolution as well as sensitivity towards CA presence is poor, it is powerful tool for routine examination in daily clinical practice. Detectors in PET and SPECT scanners also detect short wavelenght photons (γ-rays), but the

radiation source is contrast agent. In PET, short living positron emitting isotopes are used as contrast agents. Emitted positron annihilates in contact with one of surrounding electrons, resulting in two 511 keV gamma photons being emitted at 180 degrees to each other. The simultaneous emission of two photons improves spatial resolution of PET to several milimeters. Better resolution is principally impossible, as the length of positron trajectory before annihilation is also in mm scale. The PET sensitivity is excellent, just several decays from one position can be acquired. Gamma emitors (^{99m}Tc, ^{123}I, ^{131}I, ^{201}Tl, ^{111}In, ^{67}Ga) are used as contrast agents in SPECT. The SPECT sensitivity is comparable to PET, whereas spatial resolution is lower (~cm). As only CA is the source of signal in PET and SPECT, these methods are commonly combined with anatomical image from CT (Fig. 1). Therefore combined PET-CT and SPECT-CT scanners are commonly used in clinical practice.

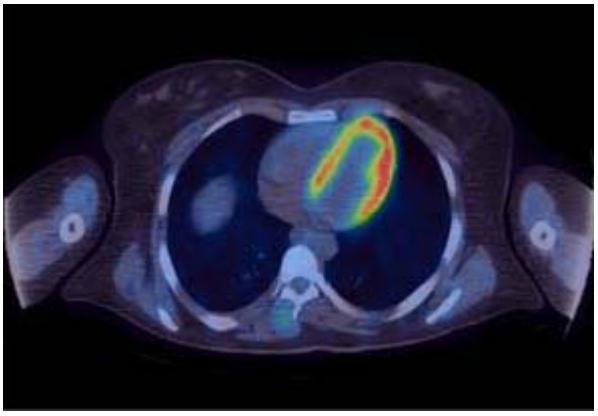

Fig. 1: Overlay of PET (yellow-red signal – horseshoe shape) and anatomical CT (blue) image of atypical neurofibroma in the right erector spinae muscle. [18F]2-fluoro-2-deoxy-D-glucose used as CA for PET[1].

Fluorescent dyes are used as contrast agents for optical imaging (OI). After CA administration, patient is enlighted with light of excitation wavelenght and emmition is observed to localize dye molecules. Sensitivity as well as spatial resolution of OI is excelent, its limiting factor is depth of tissue penetration. Light is effectively absorbed in tissue and even red light or near IR radiation, which are in so called "tissue absorption window" can reach maximally 1-2 cm thick tissue layer. Even though this is big limitation of the method, optical imaging is perfectly suitable for several applications. Very good example is the use of fluorescent labeling of tumors in surgery (Fig. 2). Use of fluorescent dyes in medical research *in-vitro* is of a great importance. Fluorescent microscopy is used for observation and allows for exact localization of dye labeled chemicals in subcellular structures.

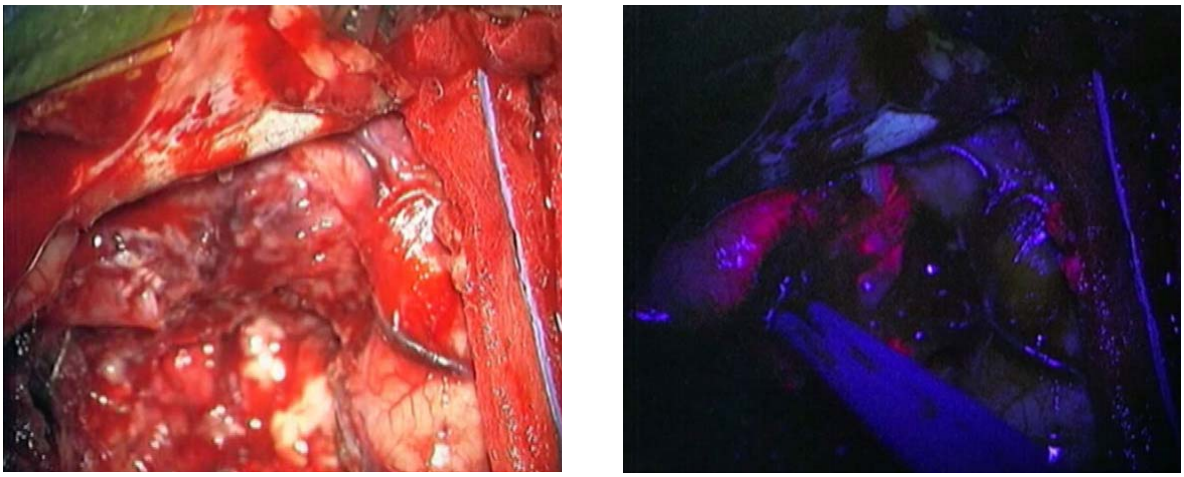

A B

Fig. 2: Fluorescence-guided surgery. It is difficult to distinguish healthy and tumoric tissue (A). Selective labeling of brain tumor with fluorescent dye (purple areas) allows to the surgeon its simple distinguishing from surrounding healthy tissue under blue light (B). Figure taken from ref. 2.

Signal in magnetic resonance imaging originates from nuclear spin relaxation of hydrogen atoms in molecule of water (not necessarily – ^{19}F[3] and hyperpolarized ^{13}C[4] and ^{129}Xe[5,6] are also used). As water is the most abundant component of human body, MRI is excellent method for displaying soft tissues (Fig. 3).

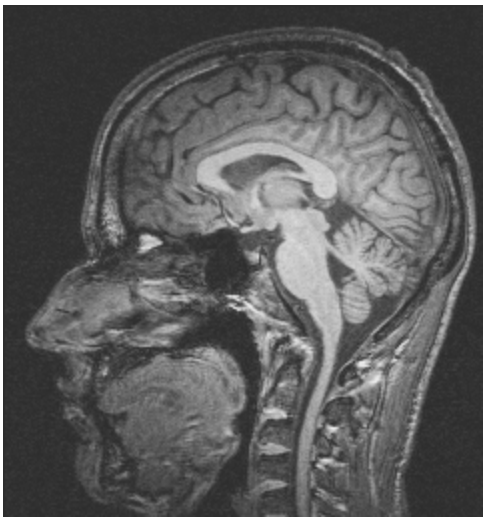

Fig 3: MRI scan of author's head

MRI scanner can resolve signals from particular parts of space with excellent resolution (~um). The intensity of signal from particular position is proportional to the water concentration and also to the rate of water spin relaxation, which is influenced by other molecules present in solution and by physical parameters of solution (*e.g.* viscosity). The contrast therefore originates from differences in these parameters among certain tissue types. Contrast agents in MRI accelerate the spin relaxation in surrounding water molecules[7]. The efficiency of MRI contrast agent, *i.e.* the rate of this acceleration is expressed in magnitude called *relaxivity*. There are two main types of contrast agent: paramagnetic ions and magnetic nanoparticles. The first mentioned is represented mainly by gadolinium(III) ions[8]. As Gd(III) is highly toxic, its stable chelates have to be used. The relaxivity of these Gd chelates is

governed by many physical parameters. One of the most important of these parameters is the rotational correlation time (τ_R), corresponding to the rate of tumbling of the complex in solution due to the thermal movement. The τ_R is determined mainly by CA molecular volume (proportional to molecular weight). In general, increasing of the molecular weight leads to slower rotation and, consequently, to higher relaxivity. The second type of MRI contrast agents is represented by magnetic nanoparticles, mostly iron oxides, usually covered with polymeric coatings (*e.g.* dextrane)[7]. The MRI sensitivity towards the presence of contrast agent is low, compared to radiomethods. On the other hand, the outstanding spatial resolution allows for displaying down to particular cells.

The progress in technology allows for sub-cellular resolution of some imaging methods (MRI, OI). Therefore, monitoring of sub-cellular assemblies or even chemical processes on molecular level became possible. This new and very promising part of research is called molecular imaging. Advanced contrast agents for molecular imaging were developed. They are able to monitor pathologies (*e.g.* tumors, inflammations) as they contain moieties which selectively bind to pathological tissue. Advanced CAs can also monitor specific chemical processes in living tissue. The intensity of CA signal change is associated with presence or absence of specific chemical process. Such so-called responsive probes sensitive to pH[9], temperature[9,10] or concentration of particular molecules[9] were already prepared.

The previous paragraphs show, that each of listed imaging techniques has its particular advantages and drawbacks, which makes it unique for specific diagnostic tasks. The combination of various imaging functionalities in one agent molecule gives rise to multimodal imaging probes. Therefore one administration of multimodal CA can be used for several different examinations. All particular CAs are combined in one system, which ensures the same distribution and therefore the results of all examinations could be evaluated together, allowing combination of advantages of particular imaging techniques. Replacing several administrations with only one is also beneficial for patient's comfort.

I.2 – Nanoscale Medical Probes

The biodistribution of medical agent is related to its molecular structure including its polarity, charge, character of charged groups, molecular size and others. These characteristics determine the pharmacokinetics of the molecule, *i.e.* whether and how fast is the molecule eliminated through liver or kidney, the ability to penetrate into tissue, affinity towards particular tissue types *etc*. Tuning the design of medical agent in order to achieve desired pharmacokinetics is a complex procedure that is in the centre of interest for many scientific teams[11,12,13].

Contrast agents of low molecular weight are mainly used in clinical practice nowadays. After administration, these compounds rapidly achieve maximum concentration in tissues (however their

uptake is usually low) which is followed by rapid clearance. Tuning of such fast pharmacokinetics is complicated. On the other hand, nanoscale objects like polymers, dendrimers, organic and inorganic particles or micelles remain longer in blood pool, which allows their accumulation in desired tissue. Their ability to penetrate into tissues as well as effective endocytosis is also documented[14]. These properties make nanoscale agents useful especially in cancer imaging. Tumor is rapidly growing tissue with high metabolical activity. The rapid growth is responsible for poor development of tumor vasculature. Capillaries in tumors are formed by poorly-aligned defective endothelial cells and therefore are "leaking", so chemicals from bloodpool can get into interstitium. Long retention times and tissue penetration ability of nanoscale objects lead to their accumulation in tumor tissue. This phenomenon is called Enhanced Permeability and Retention effect (EPR)[15].

Nanosized medical agents can be designed to have various functions in human body, including diagnosis and therapy. As an example they can be labeled with a tracer sensitive in any of imaging methods, they can bear molecular structure with specific interaction in system responsible for therapeutic effect cit., or can contain container in their structure, which is filled with low-molecular medical substance[16]. In the last case, the nanoassembly is responsible for delivery of the medical agent to the place of action and its controlled release in the place of action. The combination of these particular functions of nanoprobes in multimodal systems is a challenge of contemporary science. Such combined multimodal nanoassemblies can be used in diagnosis and treatment and the possibility of their visualization with medical imaging methods allows for the precise control of their action. The combination of all modalities in one system also ensures their equal pharmacokinetics, which is furthermore tunable due to the change of size and surface of the nanoprobe.

The nanoprobe itself can be of various chemical origins. Liposomes[17], micelles[17], linear[18] or branched polymers (*e.g.* dendrimers[19]) polymeric nanoparticles, inorganic nanoparticles and other structures were used as nanoprobes. Nanosized multimodal medical probes with inorganic nanoparticle core were widely studied[20]. Molecules responsible for various probe functions are usually attached onto the nanoparticle surface or are incorporated into the nanoparticle structure. Several types of nanoparticles can provide specific functions themselves (*e.g.* quantum dots active in optical imaging, magnetic nanoparticles active in MRI[7]). As variety of nanoparticles can form the core of the probe, various methodologies for assembling multimodal probes were developed. Most often, molecules, responsible for contrast in particular imaging methods or for targeting of the probe to desired location in body are modified with specific anchoring group which allows their connection to the nanoparticle surface. The most used anchoring group is $-Si(OR)_3$. Hydrolysis of modifying molecules containing silylester group in presence of nanoparticles (usually silica) leads to their grafting onto the surface[21,22]. The preparation of silylated precursors can be complicated and can proceed only in strictly water-free media, which might be limiting factor. Therefore another approach is often used. The particle surface is firstly modified with APS (3-(amino)propyltrialkoxysilane), resulting in silica layer containing amino groups on the nanoparticle surface. The aminogroups can be treated typically with carboxyles of modifying molecules leading to amide formation and resulting in attachment of the molecules onto the surface[23]. These methods are widely used and universal; on the other hand they

are not very convenient and simple to perform. The problem of hydrolytical stability of grafted alcylated silica shells has also been reported[24]. Many other anchoring methods were developed, mostly exploiting specific interactions between substrate and modifying molecule (*e.g.* thiols-gold surface). It appears that grafting method which is usable for wide scale of substrates, easy to perform and water compatible, giving products stable against hydrolysis, could significantly simplify preparation of multimodal medical probes with nanoparticle core as well as increase their performance. The ability of controlled simultaneous anchoring of several types of functionalities onto the surface is also beneficial.

I.3 – Adsorption of Phosphonic Acid Derivatives onto Oxidic Surfaces, Namely TiO_2

Phosphonates are intensively studied as chemical anchors[25] and have been used for modification of wide variety of surfaces like iron oxides[26], zirconium dioxide[27], aluminum oxide[27,28], oxides of rare earths[29] and other oxidic[30,31] and metal[32] substrates.

Presence of more than one phosphonate groups in the molecule can further improve sorption properties[33]. The most studied arrangement of two phosphonate groups – geminal bisphosphonate – is used in clinical practice for treatment of osteoporosis and other bone diseases[34] due to its extremely stable sorption onto the surface of bone tissue. The interaction of geminal bisphosphonates with various inorganic surfaces has been also studied in order to prepare new materials applicable for example as medical implants[35], drug delivery systems[36] or medical imaging probes[37,38].

Titanium dioxide is a highly stable, nontoxic and chemically inert material, easily preparable in form of nanoparticles. Phosphonate affinity towards the TiO_2 surface is high and the adsorption proceeds under wide variety of conditions in terms of reaction temperature, solvent and pH. Therefore it is ideal substrate for this work.

The grafting of the bisphosphonates and phosphonates[39] onto the TiO_2 surface has been studied and resulting modified materials have been used for numerous applications. Tuning hydrophilicity/hydrophobicity of the surface by organophosphonate coating may improve TiO_2 properties as a chromatographic material[40] or desirably change properties of the pores in TiO_2 membranes[41]. Also titanium alloys are always covered with a thin layer of TiO_2 and so they can be modified with organic layers in order to inhibit corrosion[42] or improve biocompatibility of bone implants[43,44]. TiO_2 nanoparticles are extensively studied for their photochemical properties and phosphonates were successfully utilized for connecting photosensing dyes to the TiO_2 surface in solar cells[45].

Description of interaction between phosphonic acid group and surface of TiO_2 on molecular level involves several possible modes of adsorption[46]. Tridentate, bidentate and monodentate adsorption

may apply depending on amount of Ti-O-P bonds formed. In the case of bi- and monodentate adsorption, the remaining oxygen atoms of the phosphonate may form hydrogen bonds with either surface hydroxyl groups or with other phosphonate groups (Scheme 1). Interpretation of experimental data and identification of participating binding modes is complicated and the results reported in literature may appear contradictory[41,46,47,48,49].

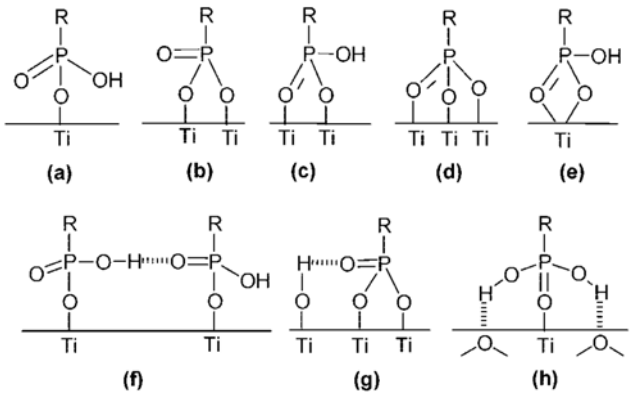

Scheme 1: Schematic representation of some possible binding modes: (a) monodentate, (b, c) bridging bidentate, (d) bridging tridentate, (e) chelating bidentate; (f-h) additional hydrogen-bonding interactions (graphics from ref. 46).

Although a lot of effort has been given to describe the sorption on molecular level, limited attention was paid to the description of the adsorption from macroscopic point of view in terms of adsorption capacity[50], hydrolytical stability[42,45,51,52,53,54] and their relation to the reaction conditions used during the sorption process.

The information about phosphonate interaction with inorganic surfaces indicate its suitability for inorganic nanoprobe preparation but it is necessary to acquire more experimental data on its adsorption behavior, before it can be used for preparation of biologically applicable nanoprobes.

Apart from number of studies of interaction between the surface of TiO_2 and phosphonic acids, many bulk titanium phosphonates were prepared[39]. The unifying motif these structures is eight-membered ring with two O-P-O connections between Ti atoms. Variability of connections between these rings results in formation of clusters (prepared only in water-free media) or in polymeric layered 2D structures and 3D networks.

There is only limited information about titanium bisphosphonates[55,56]. In reported structures, the connection among two phosphonates of the bisphosphonate moiety stabilizes the polymeric structure consisting of eight-membered Ti-O-P-O coordination rings, known from titanium-phosphonate structures.

I.4 – Photocatalytic Properties of TiO_2

TiO_2 is rigid material, which is completely inert in biological environment and therefore is ideal carrier of active molecules, adsorbed on its surface. However when TiO_2 is irradiated with UV light, electron excitation to conduction band occurs and this electron or/and its energy can be trasferred to other molecule and be responsible for chemical changes. This photocatalytic activity was demonstrated most famously by Fujisima and Honda, who constructed TiO_2 based solar couple, able to produce hydrogen and oxygen from water upon irradiation[57]. TiO_2 solar couples are intensively studied and improved up to today[58,59]. The energy of excited electron (and the hole h^+, which appears in the valence band upon excitation) can be utilized for other purposes, than solar panels or hydrogen production. In solution, oxygen and water is adsorbed on the TiO_2 surface. The excited electron interacts with O_2 molecule, forming highly reactive O_2^- species. This species undergoes further reaction with H^+ proton giving rise to $HO_2\cdot$ radical. The holes have extremely strong oxidizing effect and react with H_2O to produce $OH\cdot$ radicals or with O_2^- forming two $O\cdot$ radicals. All these highly reactive radical species are responsible for strong photooxidative properties of TiO_2 causing oxidation of molecules in its surrounding. Photooxidation is the mechanism of function of nowadays widely applied self-cleaning materials based on TiO_2 films. Radicals, which are produced upon UV irradiation, are highly toxic, which led to application of TiO_2 as an antimicrobial agent. The main interest is in water disinfection[60,61], but studies showing that TiO_2 nanoparticles can be toxic even to cancer cells[62,63,64,65] were also reported.

II. – Aim of the Work

The aim of this work is to exploit the interaction between TiO_2 surface and phosphonic acid derivatives for preparation of medical nanoprobes. Nanoparticles of TiO_2 form the core of the probe. TiO_2 is inert, biocompatible material, easily available in form of nanoparticles. Molecules, responsible for various probe functions are attached onto its surface *via* phosphonate/bisphosphonate anchor. The interaction of phosphonic acid derivatives with its surface is well known and is considered to be strong and hydrolytically stable. Therefore it appears to be perfect assembly for medical nanoprobe preparation. The goal of this project is demanding, and elaboration of suitable methodology of preparation and characterization of desired agents is necessary. Therefore the research will proceed in several consecutive steps.

II.1 – Step one: Proof of the Principle

Whole study will start with experiments designed to proof the principle. These experiments should show possibility of preparation of described probes and their advantages over medical agents used nowadays. Preparation of MRI imaging probe is the goal of this study as proposed probe design can be extremely beneficial, particularly for probes of this functionality. Grafting of Gd(III) chelates, used as MRI CAs, onto the nanoparticle surface can significantly increase their relaxivity due to the slowing down of the rotational correlation time, *i.e.* increase the contrast given by MRI probe of this design (*vide infra*). Molecule responsible for contrast in MRI containing phosphonate anchoring group in the sidechain will be prepared and grafted onto TiO_2 nanoparticle surface. It will be necessary to prepare at least moderately stable colloidal suspensions of modified nanoparticles, study their properties and compare them to the properties of free grafting molecule. Successful accomplishment of this part of the project will show whether it is possible to prepare this class of probes and if their properties are good enough to justify their further study.

II.2 – Step two: Mastering of Adsorption Process and Colloidal Stability

As products of our research are to be used in living systems, it is necessary to have colloidal solutions completely stable even under biological conditions. Any aggregation would make the product completely useless. The process of adsorption of phosphonic acid onto the TiO_2 surface was widely studied. However it is necessary to perform separate adsorption study, which should provide data about adsorption capacity and about stability of adsorbed molecules against hydrolysis, before biologically applicable probe can be prepared. Adsorption of more than one type of molecule onto the surface is also to be investigated as it opens the way towards multimodal probes. The outputs of this adsorption study are not only necessary for preparation of our medical probes, but stated parameters and their relations have never been systematically studied and therefore our findings are valuable contribution on the field of fundamental research.

II.3 – Step three: Preparation of Biologically Applicable Multimodal Probe

The results of adsorption study will allow prepration of TiO_2 nanoparticles modified with more than one type of molecules on the surface. As a proof of principle, MRI-OI imaging probe will be prepared. Combination of MRI and optical imaging in one MRI-OI probe is particularly useful. MRI has exclusive spatial resolution but rather poor sensitivity. On the other hand, optical imaging has excellent sensitivity, very good resolution, but the depth of detection is its limiting factor. Combined MRI-OI agents have big application potential in selective tumor labeling for oncological diagnosis and surgery[2,66]. This class of probes can be also effectively used for cell labeling, for example, during stem cells transplantations.

It will be necessary to prepare fluorescent dye containing phosphonic acid group in its structure. This dye and MRI active Gd(III) chelate will be anchored onto the TiO_2 surface. The study of biological properties of such prepared MRI-OI nanoprobe will be performed. The study will be focused on probe toxicity and its accumulation mechanism into the cells. It is also necessary to investigate whether probe presence can be detected by means of MRI and fluorescence. These results, obtained on selected cell models *in-vitro*, can be used for probe application *in-vivo*. The goal of the biological study is to show, whether suggested probe design is applicable for tasks of cellular imaging, namely in cell labeling and cell tracking applications.

II.4 – Step four: Exploitation of TiO_2 Photoactivity for Cancer Therapy

TiO_2 nanoparticles are suitable as a nanoparticle scaffold of medical probes, with modalities responsible for imaging or therapeutical activity attached onto its surface. Due to its unique photocatalytic properties, TiO_2 nanoparticles were already used for killing of microorganisms and even for killing of cancer cells *in-vitro*. The goal of this part of the project is to proof the cell kill ability of multimodal nanoprobe, prepared in previous step. In the case of positive results, we have multimodal probe, which is guided into tumoric tissue due to Enhanced Permeability and Retention Effect, which can serve for visualization of this tissue and which can, consequently, be responsible for tumor destruction.

III. – Discussion of the Results

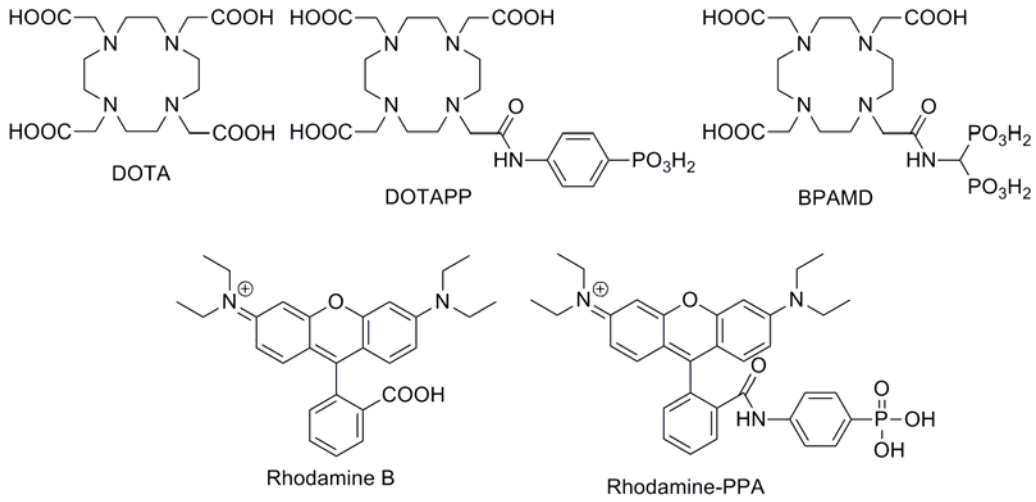

Scheme 2: Structures of compounds discussed in this work

III.1 – Step One: Proof of the Principle

(described in detail in Appendix 1)

The phosphonic acid group has been found to be very effective in anchoring different molecules to metal oxide surfaces[39,,25,,67]. The surface of titanium dioxide has been modified with a well-ordered monolayers of phosphonic acids[27,52]. Particularly, reaction of phenylphosphonic acid and its derivates with TiO_2 particles led to formation of very stable covalent Ti–O–P bonds on the surface even under mild conditions[68]. Therefore, we decided to study Gd(III) complex of a DOTA-monoamide containing a phenylphosphonate group in a pendant arm (DOTAPP) (Scheme 2) and to use it for the surface modification of TiO_2 nanoparticles. The phenylphosphonate-amide was selected as a linker, because it may be expected that its rigidity limits the local motions of the chelate. In that way optimal benefit may be obtained from the slow global tumbling of the TiO_2-DOTA conjugate and thus a significant r_1 relaxivity increase may be expected upon the conjugation of the chelate to the TiO_2 nanoparticle. As one nanoparticle can carry thousands of Gd(III) chelates, their local concentration in target tissue will be higher than in the case of low molecular MRI agents, which can help to overcome the low sensitivity for MRI as a tool for cellular and subcellular imaging.

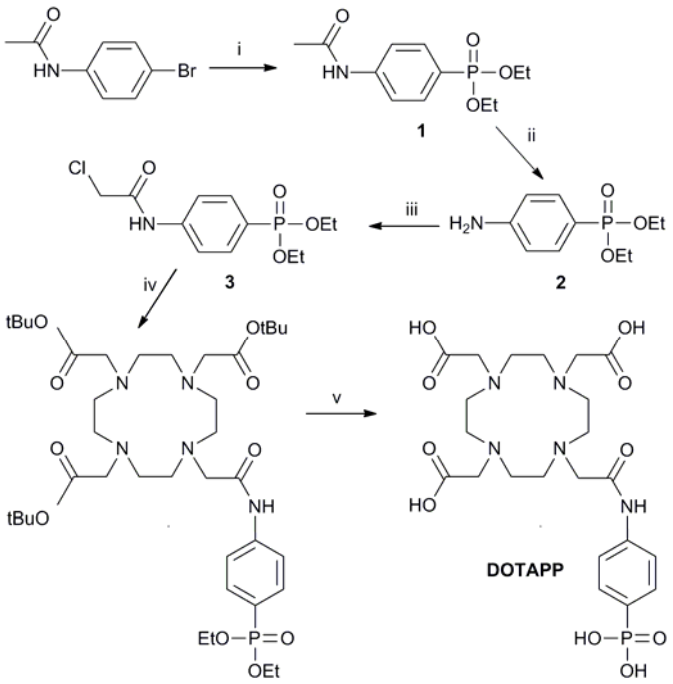

Scheme 3: Synthetic procedure for preparation of ligand DOTAPP. i) $HPO(OEt)_2$, $Pd(PPh_3)_4$, Et_3N, 90 °C, under Ar, 36 h, 58 %; ii) EtONa/EtOH, reflux, 12 h, 82 %; iii) $ClCH_2COCl$, K_2CO_3, dry MeCN, –30 °C → RT, 12 h, 97 %; iv) t-Bu_3DO_3A·HBr, K_2CO_3, dry MeCN, RT, 16 h; v) Me_3SiBr, dry MeCN, RT, 16 h, 70 % (from **3**)

III.1.1 – Ligand DOTAPP Synthesis and Properties of its Ln(III) Complexes

The ligand DOTAPP was synthesized in a good yield by a multistep procedure Scheme 3. Its lanthanide complexes were prepared by mixing of $LnCl_3$ and DOTAPP at elevated temperature, followed by slow pH increase. This procedure assures formation of "inner-cage"complexes isostructural to lanthanide complexes of DOTA. It was proven by the ^{1}H NMR spectra of the LnDOTAPP (Ln = Nd, Eu, Dy, Yb) complexes, which are very similar to those of the corresponding spectra of Ln(III) complexes of other DOTA-like ligands. Therefore, it may be concluded that the Ln(III) ions are coordinated with four nitrogen atoms and four oxygen atoms of carboxylic/amide groups forming two planes above and below the central ion.

The relaxometric properties of newly prepared ligand DOTAPP were determined. The structrual change in the ligand molecule, *i.e.* the presence of phenylphosphonate pendant arm, can cause significant changes in these properties and eventual decrease in relaxivity makes the ligand unusable for further study. The number of water molecules, directly coordinated to the Eu(III) ion (q) was confirmed to be 1 by the values of luminescence lifetimes measured for the complex in H_2O. Variable-temperature ^{17}O relaxation rates and ^{1}H NMRD profiles were measured to evaluate parameters governing relaxivity of the GdDOTAPP complex. The relaxivity – magnitude, corresponding to the efficiency of MRI contrast agent (6.17 s^{-1} mM^{-1}; 20 MHz, 298 K, pH 7.5) – was found to be higher than the value reported for the Gd(III)-DOTA complex[69], which can mainly be attributed to the slower

tumbling of the Gd-DOTAPP complex, caused by presence of bulky, rigid and highly solvated phenylphosphonate sidechain group. In summary, it can be stated, that relaxometric parameters (water reasidence time, rotational correlation time, electronic parameters – zero field splitting and electronic relaxation time, and others) of prepared GdDOTAPP complex are not far from expectations and that these complexes can be used for nanocrystalline TiO_2 modification.

III.1.1 – Adsorption of GdDOTAPP onto TiO_2 Surface

The LnDOTAPP complexes were adsorbed on the surface of nanocrystalline TiO_2 under mild conditions (70 °C, pH 3.5). No decomplexation of LnDOTAPP complexes was observed under these conditions in their ^{1}H NMR spectra. Commercial source of TiO_2 – material P 25 from Degussa company – was chosen for this study, as it is well defined, widely used and easily available. The pH appeared to be crucial for the stability of the colloidal suspensions of prepared samples. The optimal pH for the studied systems was found to be 3.5. At that pH, the colloidal suspensions are stable for at least several days. Comparison of the TEM images of the TiO_2 nanoparticles before and after sorption showed that the diameter and the shape of the nanoparticles (30–80 nm) remained unchanged. Electron diffraction patterns of both materials correspond to that of anatase. The amount of adsorbed LnDOTAPP in the prepared material was estimated using ICP-AES and corresponds to 52 μmol of complex per 1 g of TiO_2. Specific surface of used titanium dioxide is 50 m^2/g, therefore calculated area occupied by one molecule was 160 $Å^2$. Molecular modeling, used for simulation of area occupied by one molecule, gave value around 200 $Å^2$, which shows that experimental results are in good agreement with expected monolayer adsorption. The adsorbed layer exhibited also sufficient hydrolytical stability, as further washing of the material led to only negligible loss of adsorbed material (< 3 %). This suggests that stable Ti–O–P bonds have been formed (*i. e.* chemisorption),[52] since any physico-sorbed complex would have been removed during the washings applied during the synthesis of the material[68].

NMRD profile, *i.e.* dependency of relaxivity on applied magnetic field (expressed as proton Larmor frequency) was measured for the prepared material and was compared to the profile of a free complex in solution (Fig. 3) The plot shows significant relaxivity increase which occurs upon complex adsorption. The shape of the profile curve also changes – the local maximum at 20 MHz appears. The presence of the local maximum as well as relaxivity increase originates in prolongation of the rotational correlation time and was observed for Gd(III)-based contrast agents of macromolecular or nanoscale fundamental. As can be seen in Fig. 3, the relaxivity of the suspension increases upon increase of the temperature. This confirms that the relaxivity is no longer governed by the rotational correlation time, since that would be reflected in a decrease of relaxivity upon increase of temperature, due to faster thermal movement. The observed increase can be attributed to the faster exchange of water between the Gd(III) chelate and the bulk at higher temperature. For a particle with

a diameter of 30 nm with a surface fully covered with GdDOTAPP chelates, the number of Gd(III) ions per particle can be estimated to be 3300. Therefore, the relaxivity per particle is about 75 000 mM^{-1} s^{-1} (20 MHz, 25 °C).

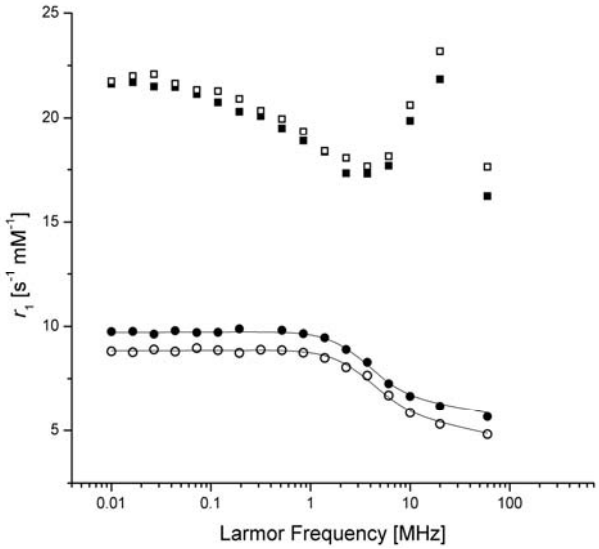

Fig. 3: 1H NMRD profiles of the GdDOTAPP complex in solution (circles) and TiO_2@GdDOTAPP suspension (squares) at 25 °C (full shapes) and 37 °C (empty shapes).

The results of the first step of the project appeared promising. The rigid phenylphosphonate linker of newly syntetized macrocyclic ligand was very efficient for anchoring the Ln(III) complexes of the ligand onto the surface of TiO_2 nanoparticles. The surface of the particles was completely covered and a strong interaction between TiO_2 surface and phosphonate results in a stable chemisorption. The nanoparticle – Gd(III) chelate based CA was prepared in effective and simple manner and its relaxometric properties were excellent. On the other hand obtained suspensions were not colloidaly stable under biological conditions. The nanoparticle polydispersity and relatively large size, which led to relatively low sorbate loads is also to be optimized. It will also be necessary to find a way to attach more than one type of molecule onto the surface in order to prepare multimodal nanoprobes.

III.2 – Step two – Mastering the Colloidal and Adsorption Chemistry

(described in detail in Appendix 2)

Adsorption of phosphonic acid derivatives onto oxidic surfaces has been widely studied topic in literature. Although a lot of effort has been devoted to description of the adsorption on molecular level, limited attention has been paid to the description of the adsorption from macroscopic point of view in terms of adsorption capacity[50], hydrolytic stability (i.e. desorption)[34,37,51,52,53,54] and their

relation to the reaction conditions used during the sorption process. The direct comparison of these properties of phosphonate and bisphosphonate is also of extreme importance for further application.

Precise quantification of adsorbed amount of phosphonate/bisphosphonate is necessary for this study. Microelemental analysis, namely ICP-AES is optimal candidate for sorption quantification as it can very precisely estimate element content in low concentrations and, further there is no interference with other components in analyzed sample. For maximal preciseness of measured data, the sorbate should contain an element, which has low natural abundance (no background, minimal risk of contamination) and is placed in third or lower period of periodical system (high sensitivity). Rare earth elements represent group with ideal properties for our purposes, but it is necessary to irreversibly incorporate them into the sorbate molecule.

DOTAPP ligand, containing phosphonate, was prepared during the first step of this project. Ligand BPAMD, containing bisphosphonate in the sidechain, was previously prepared in our laboratory and successfully used for adsorption onto the surface of hydroxyapatite.[70,71] In complexes of both ligands, lanthanide ion is extremely strongly bound in the macrocyclic cavity, whereas phosphonate groups are not involved in the coordination and remain freely available for interaction with particle surface. So, in contrast to most of phosphonate/bisphosphonate complexes having direct coordination bond between metal ion and the phosphonate groups, in this case the metal complex is an "inert" component that does not influence phosphonate sorption properties.

The evaluation of sorption properties of phosphonate and bisphosphonate provides information about relations between adsorption conditions and adsorption capacity. In addition, we studied thoroughly the hydrolytic stability of the adsorbed layer formed with both grafting groups and compared their adsorption properties. To our best knowledge, this is the first systematic study of this kind. There is limited information about the mentioned properties in literature and available data is mainly related to the macroscopic particles surfaces while our study was performed on the stable nanocolloids.

The sorption and desorption processes during the study must be performed with colloidaly stable material, as any change of aggregation state during the process can change the approachable surface of the sorbent and therefore influence the results. The methodology of adsorbing phosphonates/bisphosphonates onto the surface of nanoparticles forming stable colloids and preserving this colloidal stability during all proces of final samples preparation is necessary not only for sorption study, but also for preparation of medically applicable nanoprobes in the third step of this project. In this work, acid-stabilized colloidal nanoparticles of TiO_2 were used as a substrate and the adsorption reaction also proceeded under acidic conditions. As the study was focused on preparation of bioapplicable materials, colloidal stability of the prepared samples at physiological pH is essential. Procedure, involving several dialysis cycles and addition of polyvinylalcohol (PVA) was developed to remove excess of the sorbate and to obtain modified material as a colloid, stable at neutral pH. The procedure led to the completely transparent colloidal solutions having pH ~6.5. The prepared colloids were stable in aqueous or in the physiological (aq. 0.9 % NaCl, pH = 7.4) solutions. The results are presented as Gd/Ti ratio found by ICP-AES in the final PVA stabilized colloidal samples.

The procedure of the samples preparation is discussed frequently in this text and, thus, we introduce a standard notation of the distinct parts of the preparation process. The adsorption reaction, *i.e.* stirring of the TiO_2 with phosphonate/bisphosphonate, is called incubation. The following process, including three dialysis steps against acidified water, stabilization with PVA polymer and three dialysis steps against pure water, is called processing.

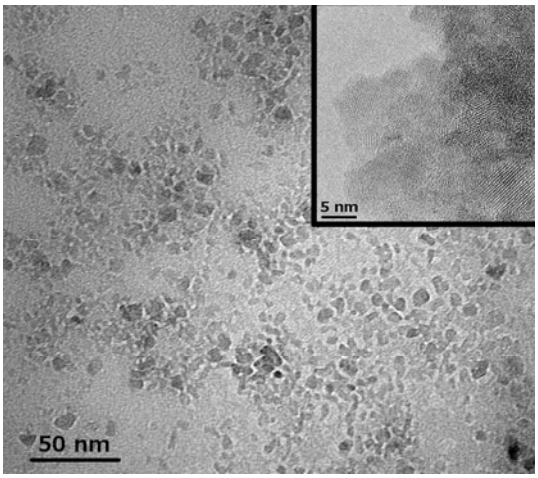

Fig. 4: TEM and HR-TEM (inset) microphotography of the studied material after incubation with bisphosphonate. The morphology of the sample is identical to morphology of unmodified material.

The particle morphology in TEM and HR-TEM microphotographs (Fig. 4) as well as electron diffraction pattern remains unchanged during incubation and processing of the samples, indicating negligible recrystallization of the bulk oxide support. This is also supported by measurement of light scattering. The results show a narrow particle size distribution that does not change upon modification with phosphonates (average particle diameter 12 nm). Similarly, we did not observe any difference in adsorbed amounts between samples stored and manipulated in dark or in daylight or fluorescent tube light, indicating a negligible photodegradation of the organic matter in presence of the photoactive anatase phase.

III.2.1 – Adsorption Capacity

A set of experiments was performed to estimate adsorption capacities of the material for phosphonate and bisphosphonate molecules. The Gd/Ti ratio found in the final samples after processing was plotted against the initial Gd/Ti ratio used for incubation. The resulting curves (not shown) exhibit a typical saturation shape. For phosphonate, the curve reaches a plateau of 27 mmol of the complex per mol of TiO_2 (337 μmol per 1 g of TiO_2). For bisphosphonate, the adsorption capacity is significantly higher as the curve reaches the plateau of 115 mmol of the complex per mol of TiO_2 (1.43 mmol per 1 g of TiO_2). Based on the BET measurements, the TiO2 particles show a surface area of 178 m2g–1 and negligible porosity. From the obtained Gd/Ti ratios and the TiO2

specific surface area, the estimated area occupied by one molecule of phosphonate and bis(phosphonate) is around 90 and 20 $Å^2$, respectively.

Based on the X-ray data, geometry of the DOTA-like complex could be averaged as a sphere having a diameter 8 Å[72] (Fig. 5). A simple geometrical model, considering such spheres and the most dense hexagonal packing, leads to a monolayer with an area of 55 $Å^2$ occupied by one molecule of the complex. Taking into account a thermal movement around the phosphonate pendant arm, experimental value of the surface occupation obtained for phosphonate (~90 $Å^2$) is in the range expected for the formation of a monomolecular layer. Results obtained for adsorption of the same phosphonate-containing complex onto a different TiO_2 matrix (Degussa P25) gave the area occupied by one molecule of the complex ~160 $Å^2$.

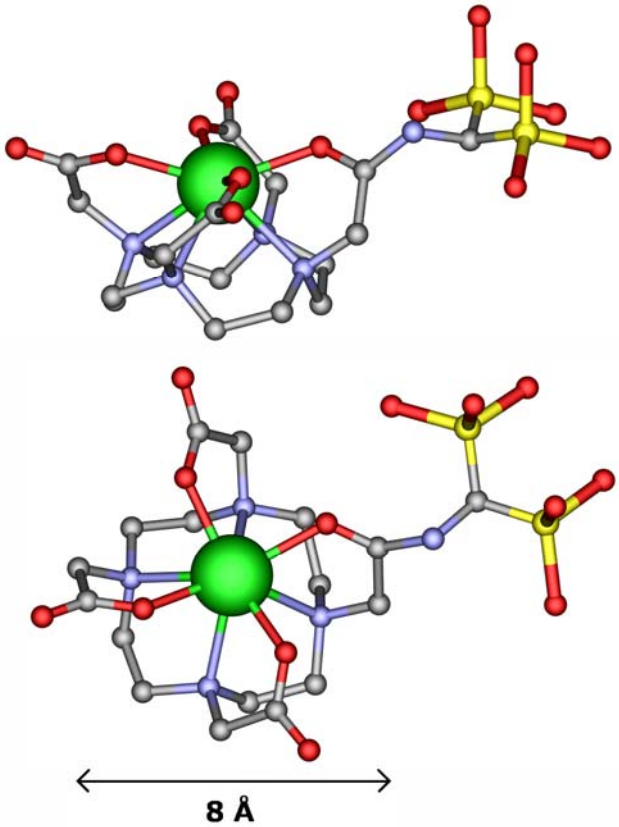

Fig. 5: Side and top views of Gd-BPAMD. The structure as well as the size of the complex are derived from the Gd-DOTA crystal structure[73] using molecular modeling. The coordinated water molecule (above the oxygen plane) and hydrogen atoms are omitted for the sake of clarity.

The experimental value for the surface occupied by one bisphosphonate-containing molecule (20 $Å^2$) is extremely small for the bulky macrocyclic complex and cannot be realistic considering the monomolecular layer formation. Several layers of the complex are more likely present on the oxide surface; one can speculate that the molecules are connected through Ti(IV) ions as a cross-linking agent into a 3D coordination polymer. Formation of such coordination polymers is reported in literature; the hydrated TiO_2 recrystallizes upon treatment with bisphosphonate under hydrothermal conditions forming a new phase. The reported crystal structures show 1D[55] and 3D[56] titanium-bisphosphonate polymers and a polyvalent interaction has been also suggested for hybrid materials

containing TiO_2 and Ti(IV)-polyphoshonates[74,75]. Such amorphous Ti-bisphosphonate 3D coordination polymer is probably present on the oxide particles surface and it is highly stable due to extensive cross-linking given by the presence of two tetrahedral phosphonate moieties in one molecule. Formation of this phase on the TiO_2 surface is enabled by the higher coordination ability of the bisphosphonate group toward hard Ti^{4+} cation if compared with that of the single phosphonate group. It has been shown that bisphosphonates are able to form with Ti^{4+} ions microporous/mesoporous materials through such 3D interaction of all donor atoms involved in the metal ion coordination and such materials are highly stable against decomposition[76].

III.2.2 – Phosphonate/Bisphosphonate Co-adsorption

Macrocyclic complexes of lanthanide(III) ions show similar physico-chemical properties along the whole lanthanide series. Thus, complexes with different metal ions should exhibit the same sorption behavior. This allows a parallel quantification of two or more complexes, each containing different lanthanide.

We studied the sorption ability of the Gd-BPAMD (the bisphosphonate) and Eu-DOTAPP (the phosphonate) complexes during co-sorption from solution containing equimolar mixture of the complexes. The Ln/Ti ratios found in the co-sorbed samples are summarized in Table 1. The values are compared to those found for the single-sorption (estimation of the adsorption capacity experiment above). The amount of adsorbed phosphonate is somewhat decreased due to the presence of bisphosphonate. But the decrease was significantly lower then that expected for a simple competition of two sorbates on the surface. Contrary, the adsorbed amount of bisphosphonate was not much affected by presence of phosphonate.

Table 1: Comparison of the Phosphonate/Bisphosphonate Single-Sorption and Co-Sorption (70 °C, pH = 2.5).

Experiment	Ln/Ti ratio used in incubation [mmol/mol]		Ln/Ti ratio found after processing [mmol/mol]	
	Phosphonate	Bisphosphonate	Phosphonate	Bisphosphonate
single-sorption	63	–	19.6	–
	-	63	–	23.1
co-adsorption	63	63	14.5	27.0
single-sorption	254	–	26.2	–
	–	254	–	104.5
co-adsorption	254	254	19.5	93.5

The sum of adsorbed bisphosphonate and phosphonate molecules exceeds the adsorbed amounts from the single-sorption experiments. This excludes the monomolecular layer formation as it would

lead to the competition of both sorbates on the surface[77]. As bisphosphonate is expected to exhibit a higher affinity towards the surface, the adsorbed amount of phosphonate would be accordingly significantly lowered. Thus, it is more likely that the phosphonate is efficiently involved in the multilayers formed by bisphosphonates during the sorption.

III.2.3 – Desorption Experiments

To determine the hydrolytic stability of the materials, they were incubated at various temperatures and the decrease of the Gd/Ti ratio as function of the dialysis time (with regular exchange of the dialyzing solution) was followed. Further, as our research is focused on bioapplicable materials, we also studied desorption in the presence of the phosphate anions as they are present in physiological fluids; the phosphate concentration was 1.5 mM and pH = 7.4 as is found in human blood plasma[78]. The presence of phosphate was expected to accelerate the desorption rate as it may compete with adsorbed phosphonate or bisphosphonate groups. The results of desorption experiments are shown in Figure 6.

For phosphonate, a significant desorption occurred during washing. The extent of desorption was lower for the samples incubated at elevated temperature. After three weeks of washing with water, the remaining amount of the sorbate varied from 34 % of the adsorbed amount found after the processing (sample incubated at 30 °C) up to 50 % (sample incubated at 90 °C). If the dialysis was performed against phosphate buffer the desorption was accelerated. Surprisingly, the adsorbed complex was not washed out completely and its amount on the oxide surface converges towards the constant value around 40 % and 15 % for the samples incubated at 90 °C and 30 °C, respectively.

The content of adsorbed phosphonate varied among the samples even before the washing experiment started – the amount of adsorbed material was increased with increasing incubation temperature (Figure 6A and 6C). The contents of sorbate in the samples during processing, measured just after the first dialysis step had no relationship to the incubation temperature. Therefore the phenomenon was explained by the fact that part of the sorbate, washed away during processing is proportional to the incubation temperature and the amount of the bound complex during incubation is probably similar at any used temperature.

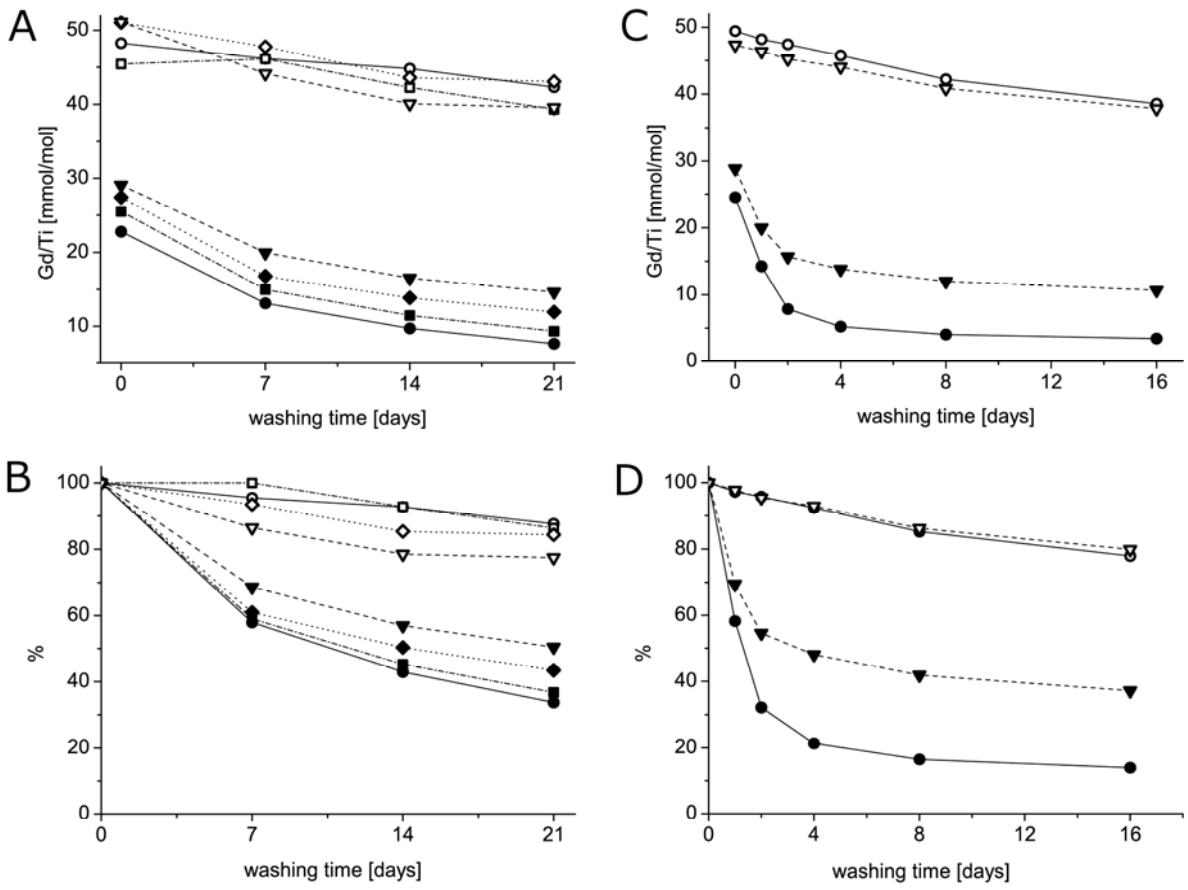

Fig. 6: Decrease of the Gd/Ti ratio as function of dialysis time for the samples containing adsorbed phosphonate (full symbols) and bisphosphonate (empty symbols) incubated at 30 °C (circles, full line), 50 °C (squares, dash-dotted line), 70 °C (diamonds, dotted line) and 90 °C (triangles, dashed line). Dialyzing solution: pure water (A – absolute vales, B – relative values); phosphate buffer (1.5 mM, pH = 7.4; C – absolute vales, D – relative values). The initial point refers to the Gd/Ti ratio in the samples after processing cycle.

The relation between incubation temperature and stability of the sorbate on the oxide surface could be explained by the existence of several modes of interaction between sorbate and sorbent surface which are energetically nonequivalent. This nonequivalency originates from different binding of adsorbed molecules, represented *e.g.* by varying hapticity of the sorbate; mono-[47], di-[48] and tridentate[41] adsorption modes of phosphonate on the TiO_2 surface have been described in literature as well as their co-existence in one material[46]. Another reason for the energetic nonequivalency can result from an occupation of energetically nonequivalent sites on the oxide surface. The slow energy-demanding transition between the mentioned binding modes towards a stronger sorbate–sorbent interactions could explain the slower desorption of phosphonate incubated at higher temperatures as more molecules of the complex should be bound by di- or tridentate modes or on energetically more convenient sites. Similar observation has been reported by Kim et al.[30] who suggested a two-step mechanism of adsorption of phosphonate-containing molecules. In the first step, contact between phosphonate and the TiO_2 surface leads to fast interaction stabilized by hydrogen bonds between the sorbate and the sorbent. The second step is the temperature-dependent rearrangement of the

hydrogen bonds into the covalent Ti–O–P bonds which are significantly stronger. The parallel existence of two or more phosphonate binding modes could also explain the "convergence" of the desorption being observed for the phosphonate samples dialyzed against phosphate buffer. From the desorption curves is evident that a part of the sorbed complexes is washed out swiftly, but the remaining sorbate resists washing. Washing of the first fraction of the sorbate proceeds with the similar rate for samples incubated at various temperatures. The remaining amount of the sorbed complex is bigger for the samples incubated at elevated temperature. This is pronounced mainly in the case of the phosphate-assisted desorption; the remaining amount of sorbate converges to 40 % for the sample incubated at 90 °C, whereas for the sample incubated at 30 °C, the curve converges to 15 % of the initial amount of the sorbate as obtained just in the end of the sample processing. This observation is in a good agreement with the presumption of the slow conversion towards the stronger binding modes (thus leading to the higher stability of surface-bound complexes) which is accelerated in the samples treated at elevated temperature during incubation.

In the case of the bisphosphonate system, the desorption was significantly slower after three weeks of washing, around 80 % of bisphosphonate remained bound on the oxide surface in each sample. Further, no dependence of the desorption rate on incubation temperature was observed. Desorption rates were uniform for all bisphosphonate samples within statistical significance. The presence of phosphate in the washing solution had a negligible effect on the desorption rate.

The explanation could be based on the fact that the presence of two binding sites in the molecule of bisphosphonate leads to a preference of the 3D multidentate binding modes (preferably tetradentate[34]) stabilizing the molecule of the complex on the surface. In the case of bisphosphonate, the stability of the coordination polymer forming the multilayers also plays an important role. It is more likely that the structure of the coordination polymer resembles structures found in titanium(IV) bisphosphonates[55,56]. In these structures, the connection among two phosphonates of the bisphosphonate moiety stabilizes the polymeric structure consisting of eight-membered Ti-O-P-O coordination rings; they are typical for phosphate and phosphonate complexes with transition metal ions. The stronger interaction of bisphosphonates in comparison with that of simple phosphonates has been pronounced in many types of interactions, *e.g.* in surface adsorption to other materials[34] or in coordination to metal ions[79].

The higher stability of the bisphosphonate multilayers is also reflected in the phosphate-assisted desorption. The desorption is not affected even in the presence of a high excess of phosphate anions in the washing solutions. This could be explained by the fact that the interaction of bisphosphonates with Ti^{4+} ions is several orders of magnitude stronger than that of phosphates.

To summarize this step of project: Colloidaly stable TiO_2 nanodispersions were used as the substrate. Macrocyclic lanthanide(III) complexes, containing phosphonate (DOTAPP) and bisphosphonate (BPAMD) in the sidechain, were adsorbed on its surface. Methodology of adsorption and further processing of the samples was developed, so that the resulting materials were prepared in the form of colloids stable under biological conditions. The systematic study of adsorption and desorption of molecules LnDOTAPP and LnBPAMD on/from the surface of anatase nanoparticles was

performed. The presence of lanthanide(III) ion in the sorbate structure allowed precise quantification of sorption *via* ICP-AES. Results showed different behavior of phosphonate and bisphosphonate groups. For phosphonate, a monomolecular layer formation was observed and the desorption rate depends on the sorption conditions. Excess of phosphate in washing media accelerates the desorption rate of the phosphonate. The bisphosphonate is adsorbed on the surface in large quantities forming multilayers which resist desorption even in the presence of phosphate ions.

III.3 – Step 3: Bioapplicable Multimodal Nanoprobe

(described in detail in Appendix 3)

As is already discussed in the introduction section of this work, the use of nanoscale probes in medicine brings several advantages in comparison with low molecular ones. Firstly it is pharmacokinetics, specific with good penetration into the tissues, effective endocytosis and relatively slow clearance, which can furthermore be tuned by probe size and surface charge[11,12,13]. In addition nanoparticles tend to accumulate in cancer tissue, which occurs due to the enhanced penetration and retention effect and is important tool in cancer diagnosis and treatment[14,15].

It was already explained, that nanoprobes can serve for various medical applications, including diagnosis and therapy. In this study, we use TiO_2 nanoparticles as a core of the probe. TiO_2 is inert, nontoxic and its photocatalytic properties can be exploited for killing of cancer cells. The surface of the particle can be modified with various molecules, ensuring particular probe functions. It was already shown during this study, that phosphonic acid derivatives are very effective TiO_2 surface modifiers. The modification can be performed in aqueous media, which is advantageous, when hydrophilic molecules like proteins are being anchored and the adsorbed layers are described to be hydrolytically stable in literature. Anchoring of contrast agent molecules for medical imaging methods leads to diagnostic nanoprobes, anchoring of drug molecules leads to therapeutic nanoprobes. One nanoparticle can carry many molecules on its surface, which leads to their high local concentration. It can be beneficial for overcoming problems with low sensitivity of some imaging methods (*e.g.* MRI). Many modalities can be combined, when preparing multimodal imaging probe. Combination of MRI and optical imaging in one MRI-OI probe is particularly useful. MRI has exclusive spatial resolution but rather poor sensitivity. On the other hand, optical imaging has excellent sensitivity, very good resolution, but the depth of detection is its limiting factor. Combined MRI-OI agents have big application potential in selective tumor labeling for oncological diagnosis and surgery[2,66]. This class of probes can be also effectively used for cell labeling, for example, during stem cells transplantations[80]. Furthermore the presence of fluorescent label allows for study of behavior of the probe in living systems by means of fluorescent microscopy.

Majority of MRI-OI imaging nanoprobes are based on iron oxide or other magnetic materials. These probes provide a negative signal in MRI, *i.e.* their presence is indicated by hypointense area (negative, T_2 contrast). These areas can be difficult to recognize and a loss of spatial resolution is occurring in the presence of CA[81]. Another approach is represented by attachment of Gd complexes on a diamagnetic core. Presence of Gd chelates results in a hyperintense area (positive, T_1 contrast) and lacks the listed disadvantages of magnetic nanoparticles. Accumulation of number of CA molecules in one entity helps overcoming the MRI sensitivity problem, furthermore, the r_1 relaxivity expressing the efficiency of MRI CA is increased upon attachment due to the slowing down of the tumbling of the chelate in solution[7].

The reported T_1 MRI and OI active inorganic nanoparticles use the cores consisting from fluorescent dye-doped silica[82], zeolite[83] nanoparticle or quantum dots[84] (usually coated by silica shell[85,86,87]). The Gd chelates are grafted onto the surface, typically by hydrolysis of their silylated derivatives[82], by amidic coupling with surface amino groups[83], building of liposome-like covers[85,86] or using avidin-biotin interactions[84]. Nanoparticles of TiO_2 were already used as a core of MRI[88], contrast agent or fluorescence labeled medical nanoprobes[89] however this is the first attempt to prepare probe of two modalities, attached to the core surface with phosphonic acid derivatives.

III.3.1 – Preparation and Properties of MRI and OI functionality

Macrocyclic ligand BPAMD, containing geminal bisphosphonate in pendant arm (Scheme 2), was prepared in our laboratory and was already used in previous part of this study[70]. The relaxation properties of GdBPAMD are within range expected for DOTA-like complexes[69].

Among many fluorescent dyes, rhodamine B was selected for several reasons: i) it is water soluble and therefore the surface of modified particles remains hydrophilic (hydrophobisation of the nanoparticle surface can lead to loss of colloidal stability). ii) its emission wavelength is in red part of the spectra, ensuring good tissue penetration. iii) rhodamine B is widely used dye and most fluorescent microscopes can be tuned for its excitation and emission parameters.

The conjugate of rhodamine B and phenyl phosphonic acid (rhodamine-PPA – Scheme 1) was prepared from rhodamine B and diethyl 4-aminophenylphosphonate. Excess of TBTU coupling agent had to be used in the first reaction step to achieve 70% conversion. The second reaction step proceeds quantitatively and no purification of the product was necessary. The change of luminescent properties occurs upon modification of the rhodamine B (Fig. 7). The excitation band moves 60 nm to the longer wavelength and the emission band moves 20 nm to the lower wavelength.

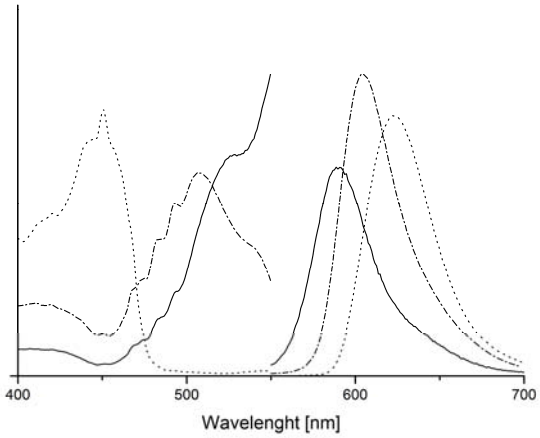

Fig. 7: Excitation (left part of the plot) and emission (right part of the plot) spectra of rhodamine B (dotted line), rhodamine-PPA (dash-dotted line) and TiO2@RhdGd (solid line). The intensities of the signals are relative and are given by the measurement conditions for each sample.

III.3.2 – Preparation and Properties of Nanoprobe TiO_2@RhdGd

Acid-stabilized colloidal TiO_2 (anatase, 12 nm diam.) was used as a substrate for adsorption. The adsorption reaction of both sorbates – Gd-BPAMD and rhodamine-PPA onto the TiO_2 nanoparticles was performed in one reaction step. The adsorption reaction proceeds under acidic conditions. Procedure, involving several dialysis cycles and addition of polyvinylalcohol (PVA) was developed to remove excess of the sorbate and to obtain modified material as a colloid of concentration 2.1 mg TiO_2@RhdGd per ml, stable at neutral pH. The procedure led to completely transparent colloids with pH ~6.5. Prepared samples were stable in water, physiological solution (0.9% NaCl, pH=7.4) and cell incubation solution.

Amount of Gd-BPAMD in TiO_2@RhdGd was estimated using ICP-AES to be 1.22 mmol of Gd-BPAMD per 1 g of TiO_2. Amount of adsorbed rhodamine-PPA was estimated indirectly by determination of its content in dialyzing solutions by means of UV-Vis. There is 0.18 mmol of rhodamine-PPA per 1 g of TiO_2.

Quantification of amount of adsorbates shows, that the complex is approximately 6.6 times more abundant on the surface, than fluorescent dye. Taking into account much lower sensitivity of MRI in comparison with OI, it is advantageous to have surface covered mainly with MRI contrast agent molecules.

The MRI properties of prepared nanoprobe were studied. The plot of millimolar r_1 relaxivity (corresponding to the MRI efficiency) vs. magnetic field is given in Fig 8.

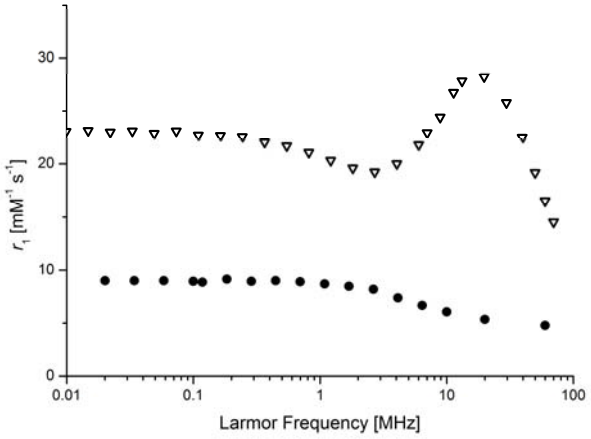

Fig. 8: ^{1}H NMRD profiles of the GdBPAMD complex in solution (circles) and TiO_2@RhdGd colloid (triangles) (measured at 25 °C)

Significant relaxivity increase in comparison with free Gd-BPAMD complex is observed. Also the shape of the curve changes and exhibits maximum at 20 MHz. The relaxivity increase as well as presence of local maximum is similar as in the case of TiO_2@GdDOTAPP in section III.1. High relaxivity values show that even though multilayers of covering molecules are present on the surface, these layers are well hydrated and water molecules can effectively approach Gd(III) complexes. Number of Gd chelates adsorbed on one 12 nm nanoparticle was calculated around 3000. Therefore r_1 relaxivity per one particle can be calculated as appx. 85 000 mmol^{-1}s^{-1} (20 MHz, 25 °C). Comparision of these values with values in III.1 shows that now, thanks to bisphosphonate hydrated multilayers, it is possible to get similar number of Gd chelates on one 12 nm nanoparticle as was on 30 nm nanoparticle, using phosphonate–anchored GdDOTAPP. The weight of 12 nm nanoparticle appx. 16 times lower than of 30 nm particle, which means, that for the same MRI contrast, one can use 1mM solution of TiO_2@RhdGd or 16 mM solution of TiO_2@GdDOTAPP. The millimolar relaxivity of TiO_2@RhdGd can be also recalculated to density of relaxivity (relaxivity of 1 g of CA in 1 L) 18 s^{-1}g^{-1}dm^3 (20 MHz, 25 °C). This value is almost three times higher than value reported for GdDOTA (6.7 s^{-1}g^{-1}dm^3, 20 MHz, 25 °C) commonly used in human medicine. The doses of MRI CAs used in clinical practice are in gram scale and, therefore, the relaxivity value, expressed with respect to weight of contrast agent, is crucial for considering its applicability. As sensitivity is the biggest MRI drawback and commonly used doses of contrast agents in mediclal practise are in gram scale, such improvement is extremely valuable.

Excitation and emission spectra of prepared probe were measured (Fig. 7). The excitation band is moved to the longer wavelengths in comparison with rhodamine-PPA and is influenced by scattering on the colloid particles at longer wavelengths. The emission band is moved even more to the shorter wavelengths ($\lambda_{Em,max}$ = 591 nm) than in the case of rhodamine-PPA.

III.3.3 – Labeling of Stem Cells

Stem cells have ability to undergo mitosis and to differentiate into cells of specific tissue. For this ability, stem cells are used in cell therapy, a very perspective branch of modern medicine research, where transplantation of stem cells into damaged tissue leads to its reparation. Tracking of the cells during and after transplantation process is essential for understanding the process as well as for successful treatment. MRI is particularly suitable technique for such tracking[90,91]. As a model for testing the suitability of our bimodal probe for stem cells labeling, we have chosen rat mesenchymal stem cells (rMSCs) as an example of adult stem cells, since they are easily derived from bone marrow, can differentiate into a variety of specialized cell populations, and are efficiently proliferated *in vitro*. The results concerning stem cells viability are of particular importance as stem cells are very sensitive towards presence of any chemical and therefore can serve as a very good test of probe biocompatibility.

The cells were labeled by cultivation for 48 h in media containing TiO_2@RhdGd agent. After incubation, the cells were washed with culture media. The viability of rMSCs labeled with TiO_2@RhdGd agent was not affected, reaching 95% and suggesting the biocompatibility (non-toxicity) of TiO_2@RhdGd agent. Also, the growth of cells in comparison with an unlabeled control was not affected. The labeling efficiency was determined by fluorescence microscopy (Fig. 9A), which showed, that more than 89 % of cells was labeled. To check the possible efflux of the internalized TiO_2@RhdGd agent out of the cells, the labeled cells (Fig. 9B) were cultured for another seven days in media not containing TiO_2@RhdGd. Even after this period of time the labeled cells were very well visible *via* fluorescence microscopy (Fig. 9C). Such long persistence of agent in cells is probably determined by nanoparticle fundamental of our probe as low molecular agents have much faster clearance. Long lasting labeling is essential for cell tracking.

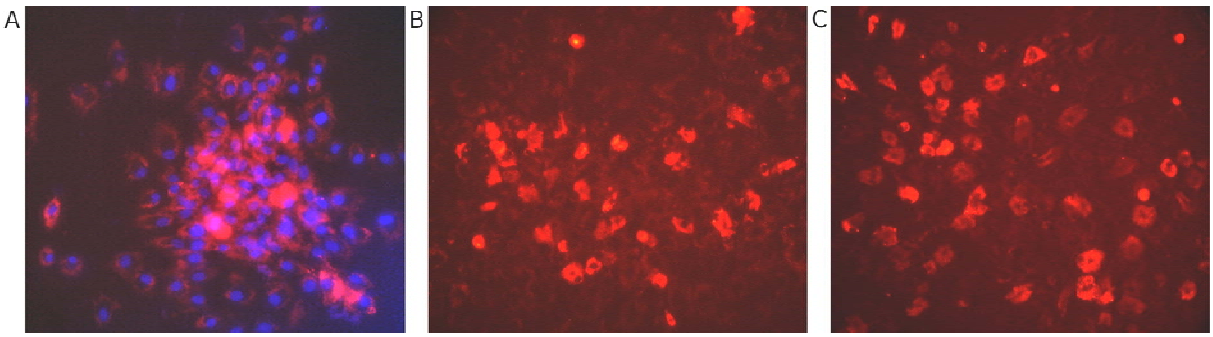

Fig. 9: Image of labeled rMSCs, obtained by fluorescence microscopy. A: TiO2@RhdGd-labeled MSCs (red) with cell nuclei co-labeled with 4',6-diamidino-2-phenylindole (DAPI – blue). B: image obtained immediately after 48h incubation with TiO2@RhdGd agent, C: Image obtained 7 days after the contrast agent was washed out. Cell nuclei were not co-labeled to avoid affecting cell viability. Scale bar 50um

Labeled cells were harvested and their suspensions were centrifuged in vials to form pellet on the bottom of the vial. A T_1-weighted MRI slice through the settled cells showed a noticeable contrast

between suspensions of the labelled and the control cells (Fig. 10A). Fluorescence camera was also used for labelled cells visualisation. The image of vial with labeled and unlabeled cells showed intensive, easily detectable fluorescence (Fig. 10B). The above stated results show very good labeling ability of our probe as well as long persistance inside the cells.

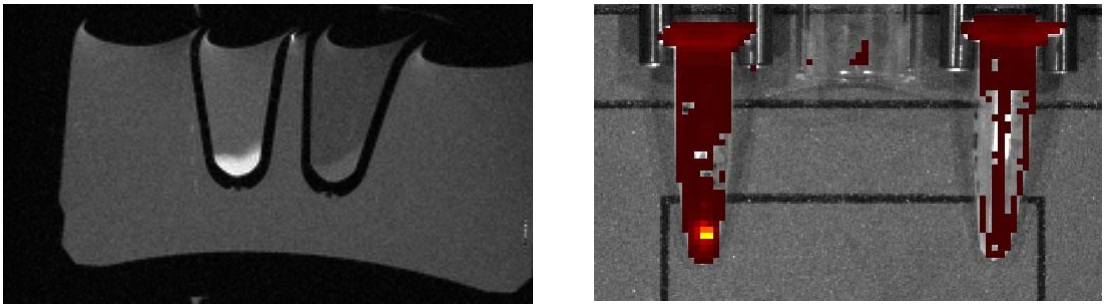

A **B**

Fig. 10: Visualization of rat mesenchymal stem cell suspensions. A: MRI slice through vials with labeled cells (left) and control (right). B: Fluorescence from labeled cells (left) and control (right)

The toxicity of TiO_2@RhdGd for stem cells was studied. The viability of labeled cells was estimated in three independent experiments (95 %) and was compared to viability of control group (97 %). Results indicate that the viability of rat stem cells is not affected by the probe presence.

The effect of presence of TiO_2@RhdGd on grow of human mesenchymal cells was studied in order to proof nontoxicity of our probe. The solution of TiO_2@RhdGd was added to cells in sixth hour, *i.e.* in proliferation curve plateau. The cells in the second experiment were incubated in the presence of TiO_2@RhdGd from the beginning. There was no effect of probe presence on cell proliferation and viability observed.

III.3.4 – Labeling of HeLa Cells

TiO_2@RhdGd probe was designed to be effective in cancer diagnosis and cancer treatment. Rapidly growing cancer tissue is very demanding on blood supply. Therefore the vascularization in solid tumor is abnormal, rapidly growing capillaries are not well developed and their walls are leaking substances to the interstitial space. Due to this leakage, together with extreme metabolical activity of carcinoma, chemicals can effectively enter the tumors in large quantities. It was documented, that nanosized objects and chemicals, which penetrate from blood circulation into the tumor are accumulating in cancer tissue and are cleared only slowly and in limited amount. This specificity of nano-objects and various polymeric molecules to accumulate in the tumor tissue is called enhanced permeability and retention (EPR) effect and is widely used in cancer diagnosis and treatment[15]. As our probe is a typical nanoparticle of a significant size, it is expected to accumulate in cancer tissue. Accumulation in the solid tumor is only prerequisite for the efficient anti-tumor activity. There must be also efficient entry of the potential anti-cancer substance/nanoparticle inside the cell. Therefore, pilot

experiments studying interaction of TiO_2@RhdGd with a typical human adenocarcinoma cell line were performed (HeLa). The experiments were designed to proof the ability of TiO_2@RhdGd to enter into the cells, the vesicular pathway of storage and accumulation inside the cell and also the ability to kill cancer cells containing TiO_2@RhdGd upon UV irradiation.

Although our probe did not exhibit toxicity on sensitive stem cells, the viability experiments on HeLa cells, which are much more robust and less sensitive to various substances toxic to the primary cell lines, were also performed, as potential toxicity can distort interpretation of consequent results. Cells were incubated in media containing TiO_2@RhdGd. DAPI (impermeable into the normal live cells) was used for identification of the damaged/dead cells. Numbers of living and dead cells were quantified using flow cytometer and compared to control group, incubated in the absence of TiO_2@RhdGd. The viability of HeLa cells was not influenced by the presence of TiO_2@RhdGd and was about 96 % in all samples.

Nanoparticles typically enter the cell *via* endocytosis using various types of endosomes. Following their trafficking inside the cell is crucial for the predictions of the time they spend inside the cell before are cleared away. Therefore we performed the co-localization studies of the fluorescent signal from internalized nanoparticles with typical markers of early and recycling endosomes (fluorescently labeled holotransferrin) and, in separate experiment, of lysosomes (anti-LAMP-1 antibody) as shown in Fig. 11.

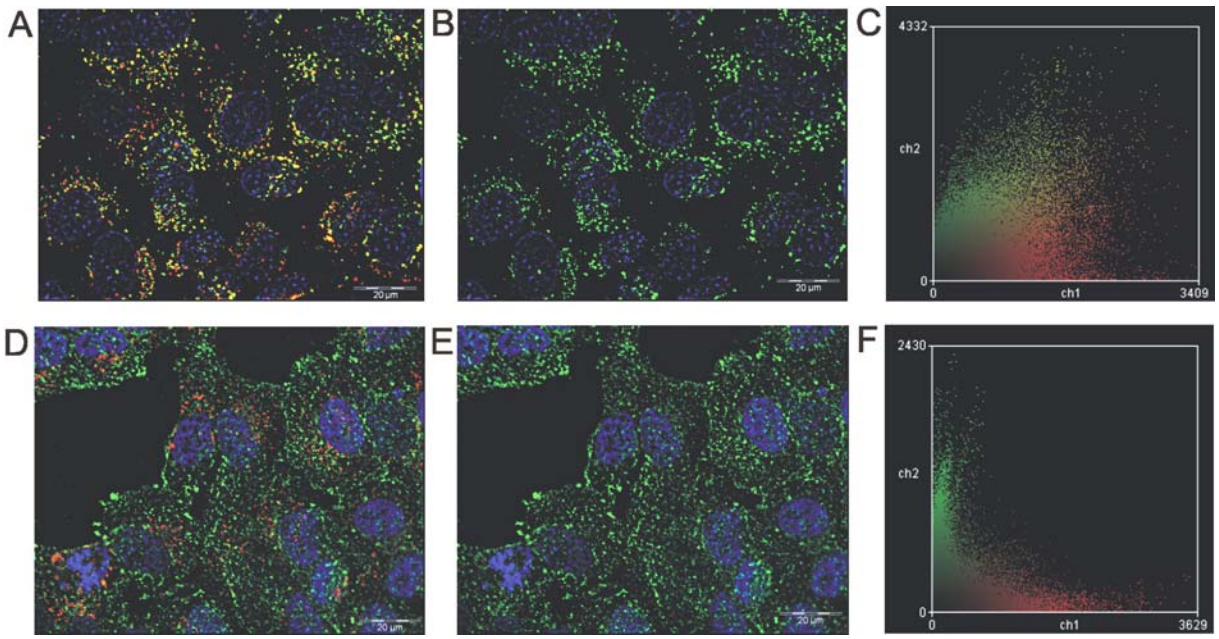

Fig. 11: Fluorescence microscopy, co-localization of nanoparticles with holotransferrin-FITC and lysosomal marker LAMP-1, nuclei stained with DAPI (blue) in all images. A: Co-localization of nanoparticles (red) with LAMP-1 (green) in HeLa cells. B: Lysosomal pattern of LAMP-1 staining only (green) in HeLa cells (displayed same sample location as in A). C: Co-localization plot (intensity of pixels in both colour channels) between nanoparticles (red) and LAMP-1 specific staining (green) exhibiting extremely high co-localization values D: Co-localization of nanoparticles (red) and holotransferrin-FITC (green) in HeLa cells. E: Localization of hotransferrin-FITC (green) in HeLa cells – typical pattern of early and recycling endosomes (displayed same sample location as in D). F: Co-localization plot between nanoparticles (red) and holotrasferrin-FITC exhibiting lack of co-localization.

The obvious overlap between the fluorescence signals of nanoparticles and Lamp-1 in Fig. 11A indicates localization of nanoparticles inside the lysosomes. The co-localization is formalized at the diagram in Fig. 11C, where fluorescence of TiO_2@RhdGd is localized on *x* axis, while LAMP-1 fluorescence on *y* axis. It is obvious, that majority of individual fluorescent events exhibit both types of fluorescence, *i.e.* majority of signal density is localized in the middle of the diagram. In contrary, position of fluorescence signals of TiO_2@RhdGd does not correspond to the signals of holotransferrin-FITC Fig. 11D and E. Again quantitative information is well visible in the diagram in Fig. 11F, where the majority of the signal density is distributed along *x* and *y* axis indicating, that only negligible amount of TiO_2@RhdGd is localized in early and recycling endosomes. The results from co-localization experiments show, that nanoparticular probe is localized exclusively in lysosomes. This means, that nanoparticles followed the endocytic pathway, were not excluded from cell via recycling endosomes and ended up and got continuously accumulated in terminally differentiated lysosomes (the same behavior exhibit dextrane probes widely used to mark lysosomal compartment). Small amount of nanoparticles localized in endosomes (co-localizing with the holotransferrin) probably belongs to the ongoing endocytic events indicating the entry pathway for the particle internalization. The results of these experiments are in a good agreement with experiments on stem cells, where one week after incubation only negligible nanoparticle clearance was observed. Successful internalization and long term storage of nanoparticles inside the cells increases their value as biomedical probes and spreads the possibilities of their application. TiO_2@RhdGd nanoparticles could be used in some special applications as non toxic fixable probes for lysosomes useful for *in-vivo* imaging.

III.3.5 – Homing of TiO_2@RhdGd Labeled Leukocytes in-vivo

As was shown and discussed before, TiO_2@RhdGd probe is non toxic, is efficiently endocytosed, enters the lysosomal storage compartment and can potentially label the appropriate cell for the long period. We tested also the potential of the TiO_2@RhdGd to become a long term probes for bi-modal (MRI/fluorescence) labeling of migratory cell populations in-vivo. We decided to use cell suspension derived from lymph nodes, to test hypothesis that primary leukocytes treated in-vitro with TiO_2@RhdGd can be introduced back in the recipient animal and that these cells are able consequently to home and find their appropriate locations in-situ in the secondary lymphoid organs. The cells derived from lymph nodes are complex suspensions (composed mostly of T- lymphocytes, together with B-lymphocytes and antigen presenting cells) containing cells with high endocytic rates. Figure 12 shows that cells endocytosed TiO_2@RhdGd probe in-vitro and after injection into the caudal vein were able to home into the original location – i.e. lymph node.

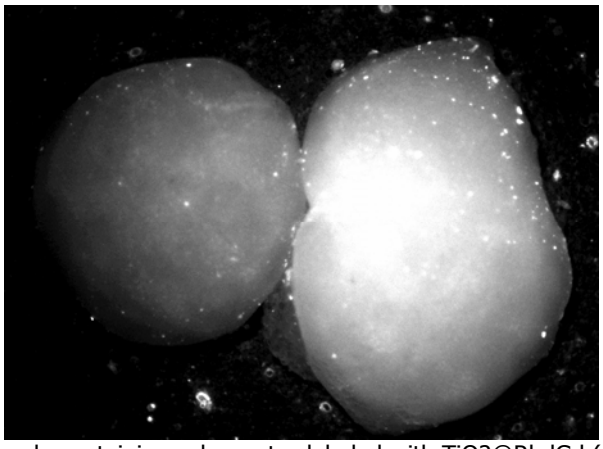

Fig. 12: Mice inguinual lymph node containing splenocytes labeled with TiO2@RhdGd (right) and control lymphnode (left). Image obtained from fluorescent binolupe.

Microscopic investigation of cryocuts prepared from inguinal lymph nodes from control mouse and from mouse injected with the TiO_2@RhdGd treated cell suspension derived from lymph nodes clearly showed that TiO_2@RhdGd treated cell population injected into recipient mouse was able to home back to lymph node. This ability was not altered by TiO_2@RhdGd and the cells could by visualized using fluorescence microscopy (Fig 13)

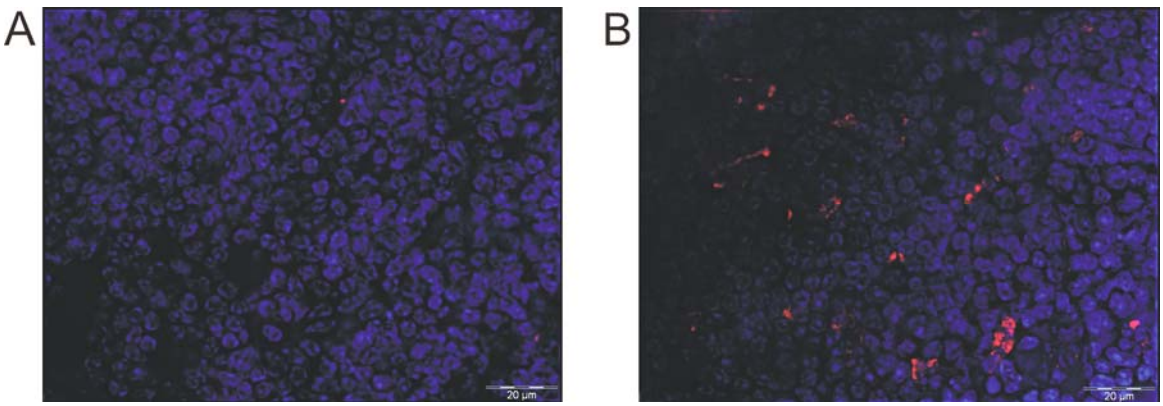

Fig. 13: Fluorescent microphotography of cryo-cutted lymph nodes - from control mouse (A) and from the mouse with injected TiO2@RhdGd labeled lymph node derived cells (B).. Red signal indicate fluorescence of TiO2@RhdGd accumulated in lysosomal compartment of homed leukocytes -., blue – nuclei labeled with DAPI.

III.3.6 – Labeling of Pancreatic Islets

Pancreatic islets (PIs) are clusters of cells, present in the pancreas, which are responsible for the production of several hormones, including the most important one, insulin. Nowadays, a very promising approach to the treatment of type 1 diabetes mellitus appears to be the transplantation of PIs into the liver[92,93]. Therefore, the tracking of PIs is one of the major topics in cellular imaging[94,95,96]. SPIO particles were used for PI labeling[8197]. As nanoparticles with slow pharmakokinetics, they allow long term labeling of islets. The drawback of SPIO use is that as T_2 agents posses so called "negative contrast" which means, that labeled islets are displayed black. It is

not easy to distinguish these black areas from anatomical structures and their quantification is also problematic. Pancreatic islets have been also labeled using MRI CAs based on simple Gd(III) chelates. It was shown that low-molecular weight Gd-based CAs efficiently accumulates in PIs[98]. The use of T_1 MRI contrast agent of nanoparticle fundament might be breakthrough in PI labeling, possessing both advantages – positive T_1 contrast as well as nanoparticle slow pharmakokinetics.

As mentioned above, pancreatic (Langerhans) islets consist of several types of cells. They are mainly α-cells (~20%, producing glucagon) and β-cells (the most abundant type, ~70%, responsible for insulin production). In addition, several other cell types are present in low abundances, including those producing other hormones (*e.g.*, somatostatin) and macrophages. To investigate which types of cells actively take up the CA (or to assess whether the CA was present only in the intercellular space of the PI), we acquired fluorescent photomicrographs of PI labeled with TiO_2@RhdGd. The results are presented in Figure14.

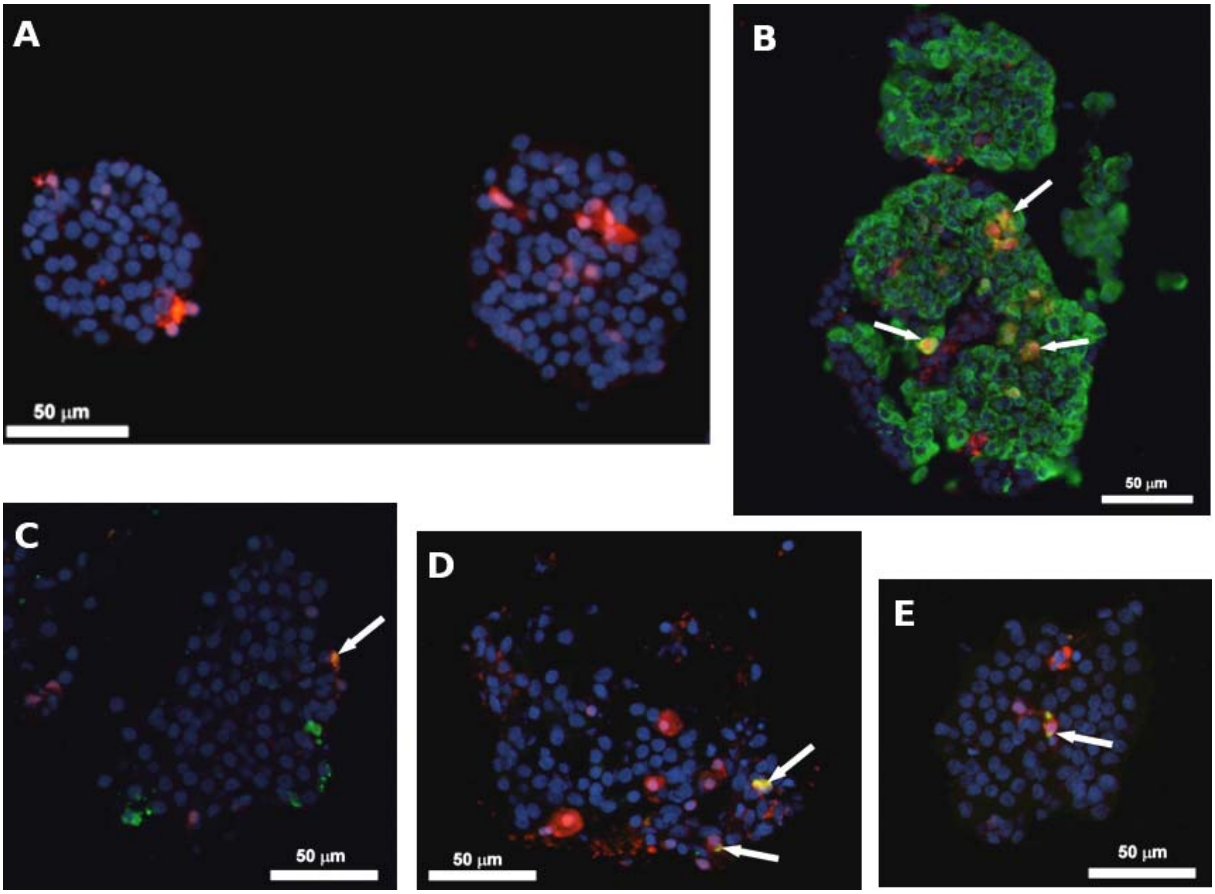

Fig. 14: Immunofluorescence staining of the contrast agent labeled PIs: **A:** Fluorescent detection of the contrast agent (red) inside the cell of pancreatic islets. **B:** Identification of islet β-cells by immunofluorescence labeling of insulin (green). Co-localization of the green insulin labeling and red contrast agent fluorescence revealed the contrast agent inside some of the beta-cells (yellow, indicated by arrows). **C:** Identification of islet α-cells by immunofluorescence labeling of glucagon (green). **D:** Co-localization of the glucagon and contrast agent (red) was rarely detected (arrow) and **E:** Identification of macrophages by immunofluorescence labeling of ED1 molecule (green). The contrast agent was detected inside of all immunodetected macrophages (arrows). The cell nuclei were counterstained by DAPI - blue fluorescence.

Figure shows the distribution of the TiO_2@RhdGd agent (red) overlaid with a visualization of karyons using standard DAPI labeling (blue). It can be seen that TiO_2@RhdGd was taken up by macrophages, α-cells, and β-cells, as indicated by the selective co-labeling of these types of cells shown in Figure 14B–D. Insulin secretion by the labeled PIs was studied by static incubation in media with low (3.3 mm) and high (22 mm) glucose levels. This revealed that insulin production was not altered by the labelling of the islets. In addition, the total viability of the cells forming PIs was found to be ~90%, showing negligible toxicity of the new CA. This study showed that the uptake of CA by pancreatic islets was sufficient to visualize individual islets by MRI. Figure 15 shows an MRI scan of a gelatine phantom with dispersed pancreatic islets. Under analogous conditions, non-labeled islets produced inferior contrast.

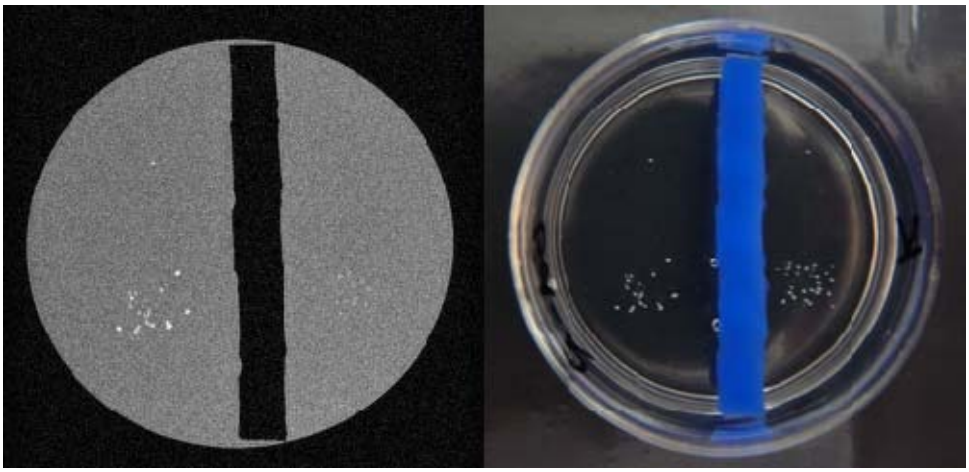

Fig.15: MRI scan of a gelatine phantom with dispersed PIs (left). Photography of the gelatine phantom (right).

Labeled PIs were injected into the liver of a rat and MRI investigation was performed. Fig. 16 displays MRI slice through rat liver with transplanted PIs. Arrows show small hyperintense areas, which most probably belong to labeled islets. Unfortunately the intensity is not high enough to confirm it with absolute certainty. Still the results of this study show high potential of TiO_2@RhdGd for PI labeling.

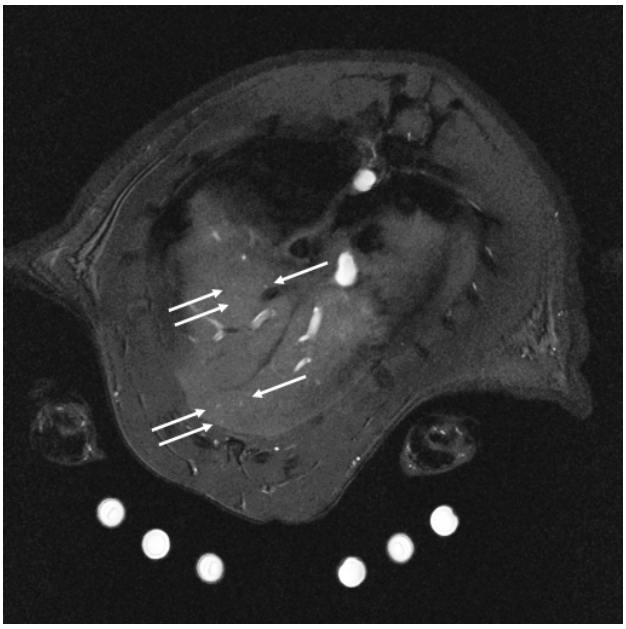

Fig.16: MRI scan of a rat liver with transplanted PIs. PI locations indicated with arrows.

III.4 – Step four: Photocatalytic activity of TiO_2@RhdGd

(described in detail in Appendix 2)

TiO_2 is rigid material, which is completely inert in biological environment. However, TiO_2 in aqueous solution produces upon UV irradiation highly toxic·OH radicals. Therefore TiO_2 nanoparticles can be potentially used for killing of cells. TiO_2 toxicity and radical production was extensively studied in water disinfection[60,61]. *In-vitro* experiments, showing ability of UV-irradiated TiO_2 to kill cancer cells is also documented[62,63,64,65]. UV light, which is essential for cell killing process, has very poor penetration depth into the tissue, which is limiting the use of this system *in-vivo.* Therefore TiO_2@RhdGd probe possesses MRI and fluorescence – diagnostic modalities, which help overcome this problem. After administration to the patient, probe is expected to be accumulated in tumor tissue. MRI examination allows for localization of the tumor and planning appropriate surgical therapy. The surgery is simplified as the fluorescence label in TiO_2@RhdGd allows for distinguishing between tumoric and healthy tissue (so called fluorescence guided surgery[2]). Consequently, UV light can be used to eradicate remaining tumor cells which could not be removed by surgery. The UV enlightenment can be performed directly in the place of tumor, avoiding shielding from surrounding tissue.

The tests of photocatalytical activity leading to cancer cell death were performed for TiO_2@RhdGd. HeLa cells were incubated in media containing TiO_2@RhdGd were extensively washed with phosphate buffer and illuminated with UV light. Absorption edge of TiO_2 is around 360 nm. As the toxicity of UV light increases with decreasing wavelength, filter from soft glass (Petri dish) was used to filter off

wavelengths under 350 nm. The illumination was performed for 7 to 20 minutes. For precise estimation of destructive UV impact, including delayed effects, cells were incubated for another three hours after illumination. Viability of harvested cells is plotted in Figure 17.

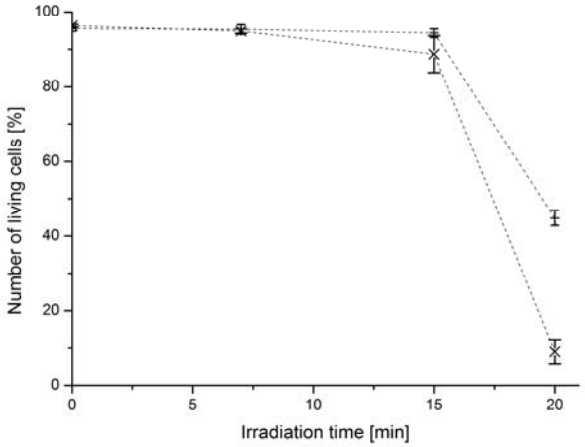

Fig. 17: Viabilities of UV illuminated cells, incubated in the presence of TiO_2@RhdGd (×) and comparison with control group (+). Experiment was performed in triplicates; errors are expressed in form of standard deviation.

The plot shows that cells labeled with nanoparticles are dying much more in longer exposure times than the cells in the control group however population in the control group also suffers from UV exposition.

IV. – Conclusion

Bimodal nanoprobe TiO_2@RhdGd combining contrast in MRI and optical imaging (OI) was prepared. Titanium dioxide nanoparticle forms the core of the probe. Photoactive properties of TiO_2 are used as an effective cell killer upon UV light irradiation. Gd(III) chelates responsible for contrast in MRI and fluorescent rhodamine B derivatives are attached to the surface using bisphosphonate/phosphonate anchor . The anchoring of Gd(III) chelate onto the surface *via* bisphosphonate leads to extraordinary high loads (1.2 mmol/1 g of TiO_2). The reason is formation of multilayers of titanium-bisphosphonate coordination polymer on the nanoparticle surface. This polymeric coating is formed in water solution, under mild conditions and is extremely resistant against hydrolysis. Furthermore phosphonate–functionalized rhodamine B derivative is incorporated into this multilayer (0.18 mmol/1 g of TiO_2), during co-adsorption of both functionalities in single reaction step. The higher abundance of MRI contrast agent on the surface in comparison with fluorescent dye takes into account low sensitivity of MRI compared to OI.

The immobilization of Gd(III) chelate on the surface leads to significant increase (up to four times) of its r_1 relaxivity (efficiency of MRI contrast agent) due to slowing of chelate tumbling in solution. The millimolar relaxivity *i.e.* relaxivity of probe solution with millimolar Gd(III) chelate concentration – 28 $mM^{-1}s^{-1}$ (20 MHz, 25 °C) – corresponds to density of relaxivity (relaxivity of 1 g of CA in 1 L) 18 $s^{-1}g^{-1}dm^3$ (20 MHz, 25 °C). This value is almost three times higher than value reported for GdDOTA (6.7 $s^{-1}g^{-1}dm^3$, 20 MHz, 25 °C) commonly used in human medicine. The doses of MRI CAs used in clinical practice are in gram scale and, therefore, the relaxivity value, expressed with respect to weight of contrast agent, is crucial for considering its applicability.

The biological properties of the prepared theranostic nanoprobe were studied *in-vitro* in several living systems including mesenchymal stem cells, adenocarcinoma HeLa cells, lymphocytes and pancreatic islets. As the fluorescent dye – rhodamine B derivative – is present in probe structure, its behavior in living systems can be tracked using fluorescence microscopy. The probe did not exhibit toxicity in any of studied systems. Nanoprobe penetrates into the cells in amount sufficient for cell tracking. Furthermore, it was shown, that the TiO_2@RhdGd remains inside cells for number of days, which is essential for cell tracking applications. Cell tracking of pancreatic islets *in-vivo* was also achieved.

Nanoparticle ability to accumulate in tumor tissue due to enhanced permeability and retention effect is well known. Although the core of the probe (photoactive TiO_2 nanoparticle) is biologically inert under normal conditions, upon UV irradiation produces highly toxic ·OH radicals, which can cause the death of surrounding living tissue. In experiment with cancer HeLa cells, it was demonstrated, that non-toxic, biocompatible probe TiO_2@RhdGd can be changed into cancer cell killer upon UV light

irradiation (λ = 350 – 400 nm). However, UV light, has very poor penetration depth into the tissue, which is limiting the use of this system *in-vivo.* Therefore, TiO_2@RhdGd probe was designed to combine MRI and fluorescence – diagnostic modalities which allow tumor localization. When the tumor position is known, the UV irradiation can be performed directly (using laparoscopic or other surgical techniques including fluorescence guided surgery), avoiding shielding from surrounding tissue. We have performed experiments, proving that the probe can visualize tissues *via* MRI and fluorescence, as well as kill cancer cells under *in-vitro* conditions.

V. – Experimental Details

Details of selected experiments are listed in following section. Other experimental details including materials and methods can be found in appropriate Appendixes.

V.1 – Preparation of Ligand DOTAPP its Ln(III) Complexes and TiO_2@GdDOTAPP (reaction scheme on page 15)

Diethyl 4-aminophenylphosphonate (2). Sodium (0.24 g, 10 mmol) was dissolved in dry EtOH (34 mL, 0.58 mol) under Ar. A solution of **1** (1.00 g, 3.6 mmol) in dry EtOH(20 mL) was added in one portion and the reaction mixture was refluxed under an argon atmosphere for 12 h. Then, the volatiles were removed with a rotavapor. The oily residue was dissolved in $CHCl_3$ (100 mL), the obtained solution was washed with H_2O (100 mL) and dried with Na_2SO_4. The $CHCl_3$ was removed by rotary evaporation. The crude product was purified by column chromatography (silica, EtOH, R_f = 0.8). Amine **2** was obtained as a white powder (0.70 g, 82 %). δ_H(400 MHz, CD_3OD) 1.29 (6H, t, $^3J_{HH}$ = 6.8 Hz, CH_2–CH_3), 4.02 (4H, m, O–CH_2), 6.71 (2H, m, C*H* arom.), 7.44 (2H, m, C*H* arom.). δ_P(121 MHz, CD_3OD) 27.4 (s)

Diethyl 4-(chloroacetamido)phenylphosphonate (3). A suspension of dried K_2CO_3 (1.26 g, 9.1 mmol) in a solution of chloroacetyl chloride (0.75 mL, 9.25 mmol) in dry MeCN (10 mL) was cooled to –30 °C and then a solution of **2** (0.70 g, 3.04 mmol) in dry MeCN (10 mL) was added dropwise. The reaction mixture was warmed up to room temperature during 3 h and then stirred overnight. The solids were filtered off and volatiles were removed by evaporation. The resulting oil was three times evaporated with toluene (10 mL) to give the crude product as yellowish crystals (0.90 g, 97 %); it was used without further purification in the next step. δ_H(400 MHz, CD_3OD) 1.32 (6H, t, $^3J_{HH}$ = 7.2 Hz, CH_2–CH_3), 4.09 (4H, m, O–CH_2), 4.21 (4H, s, Cl–CH_2), 7.77 (4H, m, C*H* arom.). δ_P(121 MHz, CD_3OD) 19.3(s)

DOTAPP 10-({N-[4-(dihydroxyphosphoryl)phenyl] carbamoyl}methyl)-1,4,7,10-tetraazacyclododecane-1,4,7-triacetic acid. Dried K_2CO_3 (0.79 g, 5.72 mmol), *t*-Bu_3DO3A·HBr (0.682 g, 1.15 mmol), crude **3** (0.367 g, 1.20 mmol) and dry MeCN (30 mL) were mixed in a 50 ml flask. The reaction mixture was stirred at room temperature for 16 h. The solids were removed

by filtration and the volatiles were removed by evaporation. The resulting yellow oil was dissolved in dry MeCN (20 mL) and trimethylsilyl bromide (3.2 g, 21 mmol) was added dropwise. The reaction mixture was stirred at room temperature for 16 h in the dark. Volatiles were removed by evaporation and the crude product was purified on cation exchange resin (Dowex 50, H+-form, elution with 5 % pyridine in water:ethanol = 1:1). The eluate was concentrated by evaporation to ~5 ml and kept at 4 °C for 16 h. The precipitate was filtered off and purified on anion exchange resin (Dowex 1, OH^--form, elution with 5 % aq. HCl). The volatiles were removed by evaporation and the resulting white powder was dried under vacuum. The product was obtained as DOTAPP·0.75HCl·4.5H_2O (0.48 g, 70 %).

(Found: C, 39.54; H, 6.46; N, 10.35; Cl, 4.08. Calcd. for : $C_{22}H_{43.75}Cl_{0.75}N_5O_{14.5}P$: C, 39.56; H, 6.60; N, 10.49, Cl, 3.98); δ_H(400 MHz, D_2O, 90 °C) 3.52 (8H, bs, C*H*$_2$ cyclen), 3.61 (8H, bs, C*H*$_2$ cyclen), 3.86 (2H, s, N–C*H*$_2$–CO), 3.99 (4H, s, N–C*H*$_2$–CO), 4.11 (2H, s, N–C*H*$_2$–CO), 7.98 (2H, m, NH–C–C*H* arom.), 7.25 (2H, m, P–C–C*H* arom.); δ_C(100 MHz, D_2O, 70 °C) 7.2 (bm), 64.4 (bs), 127.7 (s, N–C–*C*H arom.), 138.0 (d, $^2J_{CP}$ = 9.1, P–C–*C*H arom.), 143.8 (d, $^1J_{CP}$ = 14.8, P–*C* arom.), 145.6 (s, NH-*C* arom.), 178.5 (s), 181.5 (bs), 184.4 (s); δ_P (121 MHz, D_2O) 12.0 (t, $^3J_{PH}$ = 11.1 Hz)

Preparation of Ln(III) complexes of DOTAPP (General procedure). Ligand **4** (62.5 mg, 0.11 mmol) was dissolved in hot H_2O (0.5 mL). The pH of the solution was adjusted to 7.5 with 30 % aq. NaOH and then a solution of $LnCl_3 \cdot nH_2O$ (0.10 mmol) in H_2O (0.2 mL) was added dropwise. The resulting suspension of the Ln(III) phosphonate precipitate was heated at 70 °C for 12 h yielding a clear solution. The pH of this solution was adjusted to 6.5, after which the solution was heated again at 70 °C for 12 h. Then the pH was adjusted to 8.5 and the solution was heated at 70 °C overnight.

Adsorption of the Ln(III) DOTAPP complexes on the surface of TiO_2 (General procedure). TiO_2 (0.1 g, 1.25 mmol) was suspended in H_2O (50 mL) and the suspension was sonificated in an ultrasonic bath for 20 min. Then, a solution of a Ln(III) DOTAPP complex (22 μmol) in H_2O (1.5 mL) was added. The pH of the obtained suspension was adjusted to 3.5 and then it was stirred at 70 °C for 3 d followed by 4 h of cooling down to room temperature. The resulting suspension was washed with water six times. In each washing step, the suspension was concentrated from 50 to 10 ml in an ultrafiltration cell (membrane cut off – 50 kDa) and 40 ml of H_2O was added. Final volume of the suspension was 10 mL and the pH was adjusted to 3.5.

V.2 – Adsorption Study Experiments

Adsorption capacity estimation: Appropriate amount of Gd-DOTAPP (0.32–3.2 μmol) or Gd-BPAMD (0.32–12.8 μmol) solution (75 mM, pH = 2.5) was mixed with the TiO_2 colloidal solution (1 ml). The reaction mixture was stirred at 70 °C for 3 d. Reaction mixture was dialyzed three times against HCl solution (250 ml, pH 2.5) for 12 hours to remove excess of the sorbate. Then PVA solution (0.33 ml, 50 mg PVA per ml) was added and mixture was stirred in the vial for 12 h. Then, reaction mixture was dialyzed three times against pure water (250 ml) for 12 h. Resulting pH was around 6.5.

Desorption experiments: Gd-DOTAPP (3.2 μmol) or Gd-BPAMD (3.2 μmol) solution (75 mM, pH = 2.5) was mixed with TiO_2 colloidal solution (2 ml). The reaction mixture was stirred at given temperature (30, 50, 70 or 90 °C) for 3 d. Reaction mixture was dialyzed three times against HCl solution (500 ml, pH = 2.5) for 12 h to remove excess of the sorbate. Then, PVA solution (0.66 ml, 50 mg PVA per ml) was added and mixture was stirred in the vial for 12 h. Consequently, reaction mixture was dialyzed three times against pure water (500 ml) for 12 h. Resulting pH was around 6.5. The resulting colloids were further dialyzed against water or phosphate buffer (1.5 mM, pH = 7.4) at room temperature. Washing solution was exchanged every 24 h. Content of Gd and Ti in regularly collected samples was determined by ICP.

Co-adsorption experiments: Eu-DOTAPP (0.80 or 3.2 μmol) and Gd-BPAMD (0.80 or 3.2 μmol) solution (75 mM, pH = 2.5) was mixed with TiO_2 colloidal solution (1 ml). The reaction mixture was stirred at 70 °C for 3 d. Reaction mixture was dialyzed three times against HCl solution (250 ml, pH 2.5) for 12 h to remove excess of the sorbates. Then PVA solution (0.33 ml, 50 mg PVA per ml) was added and mixture was stirred in the vial for 12 h. Then, reaction mixture was dialyzed three times against pure water (250 ml) for 12 h. Resulting pH was around 6.5.

V.3 – Preparation of TiO_2@RhdGd

Preparation of Rhodamine-$PPEt_2$ conjugate. Diethyl 4-aminophenylphosphonate (96 mg, 0.42 mmol) was mixed with dimethylaminopyridine (100 mg, 0.82 mmol), *1*-(hydroxy)benzotriazole (HOBT) (56 mg, 0.57 mmol), *N,N* – (diisopropyl)ethylamine (110 mg, 0.85 mmol) and [9-(2-carboxyphenyl)-6-diethylamino-3-xanthenylidene]-diethylammonium chloride (rhodamine B) (200 mg, 0.42 mmol). The mixture was dissolved in 20 ml of dry MeCN and powder *N,N,N',N'*-tetramethyl-o-(benzotriazol-1-yl)uronium tetrafluoroborate (TBTU, 540 mg, 1.68 mmol) was added. Reaction mixture was stirred at RT in dark for 12 h. The solvent was evaporated on rotavap and product was

purified by column chromatography on silica (mobile phase – EtOAc:AcOH:EtOH = 100:2:5 {vol}; R_{ef} = 0.5). Crude product, containing remains of HOBT and diethyl 4-aminophenylphosphonate was purified by column chromatography (mobile phase – CH_2Cl_2:MeOH = 20:1) to obtain pure product in form of purple oil (yield 140 mg, 51 %).

^{1}H NMR (CD_3OD): δ = 1.11 ppm (12H, t, C*H*$_3$-CH_2-N), 1.22 (6H, td, C*H*$_3$-CH_2-O), 3.33 ppm (8H, q, C*H*$_2$-N), 4.00 ppm (4H, m, C*H*$_2$-O), 6.30 ppm (2H, d, Ar), 6.35 (1H, d, Ar), 6.38 (1H, d, Ar) 6.52 (1H, s, Ar), 6.55 (1H, s, Ar), 7.03 (2H, m, Ar), 7.08 (1H, m, Ar), 7.47−7.58 (4H, m, Ar), 7.95 (1H, m, Ar); ^{31}P{^{1}H} NMR (CD_3OD): d = 18.6; MS: calculated 654.3 observed 654.3 (M^+);

Preaparation of Rhodamine-PPA. Conjugate rhodamine-$PPEt_2$ (100 mg, 0.153 mmol) was dissolved in 5 ml of dry MeCN and trimethylsilylbromide (612 mg, 4 mmol) was added. Reaction mixture was stirred at RT in dark for 12 h. Volatiles were evaporated on rotavap. 10 ml of EtOH was added to nonvolatile residue and resulting solution was evaporated on rotavap. Procedure was repeated three times. Product was obtained in form of purple solid (89 mg, 97 %) and was not further purified. EA: Found: C, 57.11.; H, 5.90; N, 5.85; Br 10.99, 4.08. Calcd. for : $C_{34}H_{42}BrN_3O_7P^+$: C, 57.06; H, 5.92; N, 5.87, Br, 11.17). MS: calculated 598.2, observed 596.1 (M - $2H^+$). ^{1}H NMR (CD_3OD): δ = 1.16 ppm (12H, t, C*H*$_3$), 3.71 ppm (8H, q, C*H*$_2$), 6.78 ppm (2H, dd, Ar), 7.25 ppm (2H, d, Ar), 7.37 ppm (1H, m, Ar), 7.44 ppm (2H, dd, Ar), 7.55 ppm (2H, dd, Ar), 7.66 ppm (2H, d, Ar), 7.76 ppm (2H, m, Ar), 8.09 ppm (1H, m, Ar). ^{31}P{^{1}H}NMR (CD_3OD): d = 14.1 ppm (1P, s). ^{13}C{^{1}H} NMR (CD_3OD): d= 10.8 ppm (4C, s, *C*H_3), 54.9 ppm (4C, s, *C*H_2), 95.3 (1C, s, Ar) 113.2 (2C, s, Ar), 120.0 (2C, s, Ar), 123.0 (2C, s, Ar), 125.4 (2C, d, Ar), 128.0 (1C, s, Ar), 128.3 (1C, s, Ar), 131.6 (2C, d, Ar), 132.4 (2C, s, Ar), 132.7 (1C, s, Ar), 132.8 (1C, s, Ar), 133.2 (1C, d, Ar), 135.8 (1C, s, Ar), 140.0 (1C, d, Ar), 140.3 (2C, s, Ar), 152.2 (1C, s, Ar), 153.3 (2C, s, Ar), 169.1 (1C, s, C=O).

Adsorption of Ln-BPAMD and RPPA onto the TiO_2 surface. 2 mg of rhodamine-PPA (3.3 umol) was dissolved in 212 ul of 60 mM Gd-BPAMD solution (12 umol Gd-BPAMD, pH = 2.5). Resulting solution was mixed with 4 ml of TiO_2 colloidal solution. The reaction mixture was stirred at 70 °C for three days. Reaction mixture was dialyzed three times against HCl solution (1 L, pH 2.5) for 12 hours to remove excess of sorbate. Then PVA solution (1.33 ml, 66.5 mg PVA) was added and mixture was stirred in the vial for 12 hours. Then, reaction mixture was dialyzed three times against pure water (1 L) for 12 h. Resulting pH was around 6.5.

V.4 – Experiental Physical Measurements Used

Obtained products were studied using methods standardly used in organic synthesis including NMR, MS, EA. Adsorption study was evaluated using ICP-OES. Biological properties of prepared probe were followed using fluorescence microscopy and MRI. Further details can be found in appendixes.

---

1 V. S. Warbey, R. E. Ferner, J. T. Dunn, E. Calonje, M. J. O Doherty *Eur. J. Nucl. Med. Mol. Imag.* **2009**, *36*, 751–757.

2 M. Sam Eljamel *Photodiag. Photodynam. Ther.* **2008**, *5*, 260–263.

3 J. Chen, G. M. Lanza, S. A. Wickline *WIREs: Nanmed Nanobiotech* **2010**, *2*, 431–440.

4 F.A. Gallagher, M.I. Kettunen, K.M. Brindle *Prog. Nucl. Mag. Res. Sp.* **2009**, *5*, 285–295.

5 M. Das, R. W. Gunther, P. Haage *Curr. Resp. Med. Rev.* **2008**, *4*, 19–22.

6 F. Lerouge, O. Melnyk, J. Durand, L. Raehm, P. Berthault, G. Huber, H. Desvaux, A. Constantinesco, P. Choquet, J. Detour, M. Smaïhi *J. Mater. Chem.* **2009**, *19*, 379–386.

7 *The Chemistry of Contrast Agents in Medical Magnetic Resonance Imaging*, ed. A. E. Merbach and É. Tóth, Wiley, Chichester, **2001**.

8 P. Hermann, J. Kotek, V. Kubíček, I.Lukeš *Dalton Trans.* **2008**, 3027–3047.

9 M. Woods, D. E. Woessner, A. D. Sherry *Chem. Soc. Rev.*, **2006**, *35*, 500–511

10 M. Hrubý, C. Koňák, J. Kučka, M. Větřík, S. K. Filippov, D. Větvička, H. Macková, G. Karlsson, K. Edwards, B. Říhová, K. Ulbrich *Macromol. Biosci.* **2009**, *9*, 1016-1027.

11 S. Li, L. Huang *Mol. Pharmaceutics* **2008**, *5*, 496–504.

12J. Yoo, E. Chambers, S. Mitragotri *Curr Pharm Des* **2010**, *16*, 2298–2307.

13 J. D. Brain, M. A. Curran, T. Donaghey, R. M. Molina *Nanotoxicology* **2009**, *3*, 174–180.

14 A. Prokop, J. M. Davidson *J. Pharm. Sci.* **2008**, *97*, 3518−3590

15 T. Etrych, P. Chytil, T. Mrkvan, M. Šírová, B. Říhová, K. Ulbrich *J. Control. Release* **2008**, *132*, 184–192.

16 P. Debbage *Curr. Pharm. Des.* **2009**, *15,* 153–172.

17 D. Delli Castelli, E. Gianolio, S. G. Crich, E. Terreno, S. Mime *Coord. Chem. Rev.* **2008**, *252*, 2424–2443.

18 P. Lebdušková J. Kotek, P. Hermann, L. Vander Elst, R. N. Muller, I. Lukeš, J. A. Peters *Bioconjugate Chem.* **2004,** *15,* 881–889.

19 J. Rudovský M. Botta, P. Hermann, K. I. Hardcastle, I. Lukeš, S. Aime *Bioconjugate Chem.* **2006**, *17,* 975–987.

20 N. T. Thanh, L. A. Green *Nano Today* **2010**, *5*, 213–230.

21 F. Carniato, L. Tei, W. Dastrù, L. Marchese, M. Botta *Chem. Commun.* **2009**, 1246–1248.

22 W. J. Rieter, K. M. Taylor, W. Lin *J. Am. Chem. Soc* **2007**, *129*, 9852–9853.

23 J. L. Bridot, A. C. Faure, S. Laurent, C. Rivière, C. Billotey, B. Hiba, M. Janier, V. Josserand, J. L. Coll, L. Vander Elst, R. Muller, S. Roux, P. Perriat, O. Tillement *J. Am. Chem. Soc* **2007**, *129*, 5076–5084.

[24] Z. Zhang, A. E. Berns, S. Willbold, J. Buitenhuis, *J. Coll. Int. Sci.* **2007**, *310*, 446–455.

25 P. G. Mingalyov, G.V. Lisichkin *Russ. Chem. Rev.* **2006**, *75*, 541–547.

26 C. Yee, G. Kataby, A. Ulman, T. Prozorov, H. White, A. King, M. Rafailovich, J. Sokolov, A. Gedanken *Langmuir* **1999**, *15*, 7111−7115.

27 W. Gao, L. Dickinson, C. Grozinger, F. G. Morin, L. Reven *Langmuir* **1996**, *12*, 6429−6435.

28 B. Adolphi, E. Jahne, G. Busch *Anal. Bioanal. Chem.* **2004**, *379*, 646−652.

29 C. A. Traina, T. J. Dennes, J. Schwartz *Bioconjugate Chem.* **2009**, *20*, 437–439.

30 C. S. Kim, R. J. Lad, C. P. Tripp *Sens. Acutators B* **2001**, *76*, 442–448.

31 G. P. Holland, R. J. Sharma, O. Agola, S. Amin, V. C. Solomon, P. Singh, D. A. Buttry, J. L. Yarger *Chem. Mater*. **2007**, *19*, 2519−2526.

32 X. Marguerettaz, D. Fitzmaurice *Langmuir* **1997**, *13*, 6769–6779.

33 D. Portet, B. Denizot, E. Rump, J-J. Lejeune, P. Jallet *J. Colloid. Interface Sci.* **2001**, *238*, 37–42.

34 H. Fleisch *Bisphosphonates in Bone Disease, 4th Edition,* Academic Press London, **2000.**

35 I. Fishbein, I. S. Alferiev, O. Nyanguile, R. Gaster, J. M. Vohs, G. S. Wong, H. Felderman, I-W. Chen, H. Choi, R. L. Vilensky, R. J. Levy *Proc. Natl. Acad. Sci. U S A* **2006**, *103*, 159–164.

36 F. Benyettou, Y. Lalatonne, O. Sainte-Catherine, M. Monteil, L. Motte *Int. J. Pharm.* **2009**, *379*, 324−327.

37 Y. Lalatonne, C. Paris, J. M. Serfaty, P. Weinmann, M. Lecouvey, L. Motte *Chem. Commun.* **2008**, 2553–2555.

38 V. Kubíček, I. Lukeš *Future Med. Chem.* **2010**, *2*, 521–531.

39 A. Vioux, J. Le Bideau, P. H. Mutin, D. Leclerq *Top. Curr. Chem.*, **2004**, *232*, 145–174.

40 D. H. Taffa, M. Kathiresan, L. Walder *Langmuir* **2009**, *25*, 5371–5379.

41 J. Randon, P. Blanc, R. Paterson *J. Membr. Sci.* **1995**, *98*, 119−129.

42 E. Jaehne, S. Oberoi, H.-J. P. Adler *Prog. Org. Coat.* **2008**, *61*, 211–223.

43 J. Schwartz, M. J. Avaltroni, M. P. Danahy, B. M. Silverman, E. L. Hanson, J. E. Schwarzbauer, K. S. Midwood, E. S. Gawalt *Mater. Sci. Eng. C* **2003**, *23*, 395−400.

44 J. Beuvelot, D. Portet, G. Lecollinet, M.-F. Moreau, M. F. Basle *J. Biomed. Mater. Res. B* **2009**, *90B*, 873–881.

45 E. Bae, W. Choi, J. Park, H. S. Shin, S. B. Kim, J. S. Lee *J. Phys. Chem. B* **2004**, *108*, 14093–14101.

46 F. Brodard-Severac, G. Guerrero, J. Maquet, P. Florian, C. Gervais, P. H. Mutin *Chem. Mater.* **2008**, *20,* 5191–5196.

47 P. Raghunath, M. C. Lin *J. Phys. Chem. C* **2009**, *113*, 8394–8406.

48 S. Pawsey, M. McCormick, S. De Paul, R. Graf, Y. S. Lee, L. Reven, H. W. Spiess *J. Am. Chem. Soc.* **2003**, *125*, 4174–4184.

49 R. Luschtinetz, J. Frenzel, T. Milek, G. Seifert *J. Phys. Chem. C* **2009**, *113*, 5730–5740.

50 C. Viorney *Surface functionalisation of titanium with phosphonated ligands to improve bone bonding* Ecole Polytechnique Federale de Lausanne: Laussane, Switzerland, **2000.**

51 J. J. Shephard, S. A. Dickie, A. J. McQuillan *Langmuir* **2010**, *26*, 4048−4056.

52 S. Marcinko, A. Y. Fadeev, *Langmuir* **2004**, *20*, 2270–2273.

53 E. S. Gawalt, M. J. Avaltroni, N. Koch, J. Schwartz *Langmuir* **2001**, *17*, 5736–5738.

54 M. P. Danahy, M. J. Avaltroni, K. S. Midwood, J. E. Schwarzbauer, J. Schwartz *Langmuir* **2004**, *20*, 5333−5337.

55 C. Ninclaus, C. Serre, D. Riou, G. Ferey *C. R. Acad. Sci., Ser IIc: Chim.* **1998**, *1*, 551−556.

56 C. Serre, G. Ferey *Inorg. Chem.* **1999**, *38*, 5370−5373.

57 A. Fujishima, K. Honda *Nature* **1972**, *238*, 37–38.

58 M. K. Nazeeruddin, A. Kay, I. Rodicio, R. Humphry-Baker, E. Mueller, P. Liska, N. Vlachopoulos, M. Grätzel *J. Am. Chem. Soc.* **1993**, *115*, 6382–6390.

59 Y. Chiba, A. Islam, Y. Watanabe, R. Komiya, N. Koide, L. Han *Jap. J. App. Phys.* **2006**, *45*, L638–L640.

60 M. Farshbaf Dadjour, C. Ogino, S. Matsumura, S. Nakamura, N. Shimizu *Water Res.* **2006**, *40*, 1137–1142.

61 F. M. Salih *J. App. Microbiol.* **2002**, *92*, 920–926.

62 R. Cai, Y. Kubota, T. Shuin, H. Sakai, K. Hashimoto, A. Fujishima *Cancer Res.* **1992**, *52*, 2346–2348.

63 N. Huang, X. Min-hua, C. Yuan, Y. Rui-rong *J. of Photochem. Photobiol. A* **1997**, *108*, 229–233.

64 S. Ivanković, M. Gotić, M. Jurin, S. Musić *J. Sol-Gel Sci. Techn.* **2003**, *27*, 225–233.

65 M. Kalbáčová, J. M. Macak, F. Schmidt-Stein, C. T. Mierke, P. Schmuki *Phys. Stat. Sol. (RRL)* **2008**, *2*, 194–196.

66 R. Trehin, J.-L. Figueiredo, M. J. Pittet, R. Weissleder, L.Josephson, U. Mahmood *Neoplasia* **2006**, *8*, 302−311.

67 B. Bujoli, H. Roussiere, G. Montavon, S. Laib, P. Janvier, B. Alonso, F. Fayon, M. Petit, D. Massiot, J-M. Bouler, J. Guicheux, O. Gauthier, S. M. Lane, G. Nonglaton, M. Pipelier, J. Leger, D. R. Talham, C. Tellier *Prog. Solid State Chem.* **2006**, *34*, 257–266.

68 G. Guerrero, P. H. Mutin, A. Vioux *Chem. Mater.*, **2001**, *13*, 4367–4373.

69 D. H. Powell, O. M. N. Dhubhghaill, D. Pubanz, L. Helm, Y. S. Lebedev, W. Schlaepfer, A. E. Merbach *J. Am. Chem. Soc.*, **1996**, *118*, 9333–9346.

70 V. Kubíček, J. Rudovský, J. Kotek, P. Hermann, L. Vander Elst, R. N. Muller, Z. I. Kolar, H. T. Wolterbeek, J. A. Peters, I. Lukeš *J. Am. Chem. Soc.* **2005**, *127*, 16477–16485.

71 T. Vitha, V. Kubíček, P. Hermann, Z. I. Kolar, H. T. Wolterbeek, J. A. Peters, I. Lukeš *Langmuir* **2008**, *24*, 1952–1958.

72 F. Benetollo, G. Bombieri, L. Calabi, S. Aime, M. Botta *Inorg. Chem.* **2003**, *42*, 148–157.

73 J.-P. Dubost, J.-M. Leger, M.-H. Langlois, D. Meyer, M. Schaefer *C. R. Acad. Sci. Ser. II* **1991**, *312*, 349–351.

74 X.-J. Zhang, T.-Y. Ma, Z.-Y. Yuan *Eur. J. Inorg. Chem.* **2008**, 2721–2726.

75 X.-J. Zhang, T.-Y. Ma, Z.-Y. Yuan *J. Mater. Chem.* **2008**, *18*, 2003–2010.

76 T.-Y. Ma, X.-Z. Lin, Z.-Y. Yuan *Chem. Eur. J.* **2010**, *16*, 8487–8494.

77 M. P. Danahy, M. J. Avaltroni, K. S. Midwood, J. E. Schwarzbauer, J. Schwartz *Langmuir* **2004**, *20*, 5333−5337.

78 G. J. Kemp, A. Btumsohn, B. W. Morris *Clin. Chem.* **1992**, *38*, 400−402.

79 NIST Standard Reference Database 46 (Critically Selected Stability Constants of Metal Complexes), Version 8.0, **2004**

80 Z. Kotková, J. Kotek, D. Jirák, P. Jendelová, V. Herynek, Z. Berková, P. Hermann, I. Lukeš *Chem. Eur. J.* **2010**, *16*, 10094–10102.

81 J. Kříž, D. Jirák, D. White, P. Foster *Transplantation Proceedings* **2008**, 40, 444–448.

82 W. J. Rieter, J. S. Kim, K. M. L. Taylor, H. An, Wei. Lin, T. Tarrant, Wen. Lin *Angew. Chem. Int. Ed.* **2007**, *46*, 3680–3682.

83 M. Tsotsalas, M. Busby, E. Gianolio, S. Aime, L. De Cola *Chem. Mater.* **2008**, *20*, 5888–5893.

84 L. Prinzen, R.-J. J. H. M. Miserus, Anouk Dirksen, T. M. Hackeng, N. Deckers, N. J. Bitsch, R. T.A. Megens, K. Douma, J. W. Heemskerk, M. E. Kooi, P. M. Frederik, D. W. Slaaf, M. A. M. J. van Zandvoort, C. P. M. Reutelingsperger *Nano Lett.* **2007**, *7*, 93−100.

85 W. J. M. Mulder, G. J. Strijkers, G. A. F. Van Tilborg, D. P. Cormode, Z. A. Fayad, K. Nicolay *Acc. Chem. Res.* **2009**, *42*, 904−914.

86 D. Gerion, J. Herberg, R. Bok, E. Gjersing, E. Ramon, R. Maxwell, J. Kurhanewicz, T. F. Budinger, J. W. Gray, M. A. Shuman, F. F. Chen *J. Phys. Chem. C* **2007**, *111*, 12542–12551.

87 R. Koole, M. M. van Schooneveld, J. Hilhorst, K. Castermans, D. P. Cormode, G. J. Strijkers, C. de M. Donega, D. Vanmaekelbergh, A. W. Griffioen, K. Nicolay, Z. A. Fayad, A. Meijerink, W. J. M. Mulder *Bioconjugate Chem.* **2008**, *19*, 2471–2479.

88 P. J. Endres, T. Paunesku, S. Vogt, T. J. Meade, G. E. Woloschak, *J. Am. Chem. Soc*. **2007**, *129*, 15760–15761.

89 K. T. Thurn, T. Paunesku, A. Wu, E. M. B. Brown, B. Lai, S. Vogt, J. Maser, M. Aslam, V. Dravid, R. Bergan, G. E. Woloschak *Small* **2009**, *5*, 1318–1325.

90 D. L. Kraitchman, W. D. Gilson, C. H. Lorenz *J. Mag. Res. Imag.* **2008**, *27*, 299–310.

91 A. S. Arbab, J. A. Frank *Regener. Med.* **2008**, *3*, 199–215.

92 A. Hogan, A. Pileggi, C. Ricordi, *Front. Biosci.* **2008**, *13*, 1192–1205.

93 V. Vaithilingam, G. Sundaram, B. E. Tuch *Curr. Opin.Organ Transplant.* **2008**, *13*, 633–638.

94 M. Woods, S. Zhang, A. D. Sherry *Curr. Appl. Phys. Curr. Med. Chem. – Immunol. Endocrin. Metabol. Agents* **2004**, *4*, 349–369.

95 A. Moore *Eur. J. Radiol.* **2009**, 70, 254 –257.

96 Z. Medarova, A.Moore *Nat. Rev. Endocrin.* **2009**, *5*, 444–452.

97 D. Jirák, J. Kříž, V. Herynek, B. Andersson, P. Girman, M. Burian, F. Saudek, M. Hájek *Magn. Reson. Med.* **2004**, *52*, 1228–1233.

98 L. Biancone, S. Geninatti Crich, V. Cantaluppi, G. M. Romanazzi, S.Russo, E. Scalabrino, G. Esposito, F. Figliolini, S. Beltramo, P. C.Perin, G. P. Segoloni, S. Aime, G. Camussi *NMR Biomed.* **2007**, *20*,40–48.